HHS Public Access

Author manuscript

Neuron. Author manuscript; available in PMC 2019 May 14.

Published in final edited form as:

Neuron. 2018 November 07; 100(3): 593–608.e3. doi:10.1016/j.neuron.2018.09.008.

Oxytocin Transforms Firing Mode of CA2 Hippocampal Neurons

Natasha N. Tirko[1,4], **Katherine W. Eyring**[1,4], **Ioana Carcea**[1,2,3], **Mariela Mitre**[1,2,3], **Moses V. Chao**[1,2], **Robert C. Froemke**[1,2,3], and **Richard W. Tsien**[1,5,*]

[1]NYU Neuroscience Institute, New York University School of Medicine, New York, NY 10016, USA

[2]Skirball Institute, New York University School of Medicine, New York, NY 10016, USA

[3]Department of Otolaryngology, New York University School of Medicine, New York, NY 10016, USA

[4]These authors contributed equally

[5]Lead Contact

SUMMARY

Oxytocin is an important neuromodulator in the mammalian brain that increases information salience and circuit plasticity, but its signaling mechanisms and circuit effect are not fully understood. Here we report robust oxytocinergic modulation of intrinsic properties and circuit operations in hippocampal area CA2, a region of emerging importance for hippocampal function and social behavior. Upon oxytocin receptor activation, CA2 pyramidal cells depolarize and fire bursts of action potentials, a consequence of phospholipase C signaling to modify two separate voltage-dependent ionic processes. A reduction of potassium current carried by KCNQ-based M channels depolarizes the cell; protein kinase C activity attenuates spike rate of rise and overshoot, dampening after-hyperpolarizations. These actions, in concert with activation of fast-spiking interneurons, promote repetitive firing and CA2 bursting; bursting then governs short-term plasticity of CA2 synaptic transmission onto CA1 and, thus, efficacy of information transfer in the hippocampal network.

In Brief

Tirko et al. show that activation of oxytocin receptors drives pyramidal cells in hippocampal area CA2 to fire bursts. They deconstruct the cellular mechanism, oxytocin receptor-driven modulation of K+, and spike-generating currents and reveal the circuit consequences for neurotransmission to CA1.

*Correspondence: richard.tsien@nyumc.org.

AUTHOR CONTRIBUTIONS

N.N.T., K.W.E., and R.W.T. designed the research. N.N.T. and K.W.E. performed experiments and analyzed data. M.M., M.V.C., and R.C.F. contributed reagents and tissue. I.C. provided the images in Figures 1A and S1A and performed stereotaxic injections in the PVN. N.N.T., K.W.E., and R.W.T. wrote the paper with contributions from M.M., I.C., R.C.F., and M.V.C.

DECLARATION OF INTERESTS

The authors declare no competing interests.

SUPPLEMENTAL INFORMATION

Supplemental Information includes eight figures and can be found with this article online at https://doi.org/10.1016/j.neuron.2018.09.008.

INTRODUCTION

Neuromodulation, an essential property of the brain, greatly diversifies the flexibility of neurons and circuits (Bargmann and Marder, 2013; Kaczmarek and Levitan, 1987; Siegelbaum and Tsien, 1983). Neuromodulators can alter intrinsic firing properties (e.g., Cantrell and Catterall, 2001) as well as synaptic transmission, sometimes transforming cells from quiet to bursting, reshaping circuit function (Marder, 2012) and expanding the repertoire of responses to changes in internal state and external environment.

Here we examine the neuromodulatory effects of oxytocin on neurons in hippocampal area CA2 and their output in CA1. Oxytocin is a highly conserved peptide neuromodulator important for promoting sexual, maternal, and complex social behaviors (Ferguson et al., 2001; Marlin et al., 2015; Nishimori et al., 2008) and increasing positive social interaction and trust in humans (Baumgartner et al., 2008. Disruptions in oxytocin signaling contribute to neurological disorders; reductions in serum oxytocin and genetic links to the oxytocin receptor (OXTR) gene have been found in autistic patients (Jacob et al., 2007; Modahl et al., 1998; Wu et al., 2005), and altered oxytocin serum levels (Striepens et al., 2011) and reduced OXTR expression (Uhrig et al., 2016) are found in schizophrenic patients. Mice lacking oxytocin or OXTR display impaired sociability and social memory (Choe et al., 2015; Ferguson et al., 2001; Lin et al., 2018; Nishimori et al., 2008; Pobbe et al., 2012; Raam et al., 2017; Sala et al., 2011), and oxytocin delivery improves social behavior in mouse models of Autism spectrum disorder (ASD) (Peñagarikano et al., 2015). This diversity of function can be attributed in part to patterns of OXTR expression, recently explored with a novel anti-OXTR antibody (Mitre et al., 2016). Clarification of regional receptor expression spurs efforts to learn how OXTR stimulation alters ion channel activity, cellular responses, and circuit dynamics.

Here we describe oxytocin modulation in hippocampal area CA2, a small but distinctive region flanked by CA3 and CA1 (Lorente De Nó, 1934). Overlooked for decades, area CA2 has recently emerged as functionally important and clinically relevant. CA2 exhibits distinct gene expression, connectivity, and electrophysiology (Chevaleyre and Siegelbaum, 2010; Cui et al., 2013; Dudek et al., 2016; Jones and McHugh, 2011; Kohara et al., 2014; Piskorowski and Chevaleyre, 2013; Zhao et al., 2007). In rodents, CA2 output is essential for social memory formation (Hitti and Siegelbaum, 2014; Lin et al., 2018; Raam et al., 2017). CA2 place cells remap in response to context changes, social stimulation, and time (Alexander et al., 2016; Lu et al., 2015) and fire high-frequency bursts *in vivo* (Kay et al., 2016). Additionally, changes in CA2 morphology are associated with schizophrenia and age-related dementia in both human patients and animal models (Chevaleyre and Piskorowski, 2016).

Given the likely importance of CA2 in social cognition, we wondered how oxytocin might modulate CA2 cellular and synaptic responses. CA2 and CA3 are hotspots for OXTR expression (Mitre et al., 2016), and oxytocin signaling there participates in social recognition (Lin et al., 2018; Raam et al., 2017). Previous studies have described CA2 modulation by vasopressin, another peptide hormone important for social behavior (Pagani

et al., 2015). However, little is known about which type(s) of cells are targeted by oxytocin and how their responses lead to changes in hippocampal circuit function.

Our experiments revealed a robust modulation of excitatory pyramidal cells in CA2. OXTRs caused phospholipase C (PLC) activation and launching of two divergent signaling mechanisms, one leading to reduction in K^+ conductance and the second acting through protein kinase C (PKC) and intracellular Ca^{2+} to modify the rapid conductance underlying spikes. OXTR activation also modulated fast-spiking interneurons in CA2, as is the case in CA1 (Owen et al., 2013). Together, these signaling actions were necessary and sufficient to generate high-frequency action potential bursts in CA2 pyramidal cells. Through modulation of the timing and frequency of CA2 bursting, oxytocin induces short-term synaptic plasticity to tune excitatory and inhibitory output onto CA1. Thus, oxytocin modulation of multiple signaling pathways and diverse cell types operates in coordination to tune the effect of CA2 on the hippocampal network.

RESULTS

CA2 Pyramidal Cells Express OXTR and Receive Oxytocinergic Input

To label OXTR-bearing cells, we crossed *Oxtr cDNA^{HA}-Ires-Cre* mice (Hidema et al., 2016) with Cre-dependent TdTomato reporter mice *(Ai14)* (Madisen et al., 2010). Fluorescence images of cortical sections showed striking labeling of CA2 pyramidal neurons (Figure 1A), considerably more than CA1 pyramids but comparable with CA3 pyramidal cells. No differences in OXTR expression were observed between male (Figure 1A) and female mice (Figure S1A).

In parallel immunohistochemical experiments (Figure 1B), CA2 pyramidal cells were identified by staining for RGS14, a G-protein regulator expressed in these neurons (Evans et al., 2014; Lee et al., 2010). Using a highly specific antibody, OXTR-2 (Mitre et al., 2016), we found that ~96% of RGS14+ CA2 pyramidal cells also co-express OXTRs (N = 2 animals). OXTR-2 immunoreactivity was detected in neighboring CA3 neurons but only in 10% of nearby CA1 cells (Figures 1B and S1D).

To identify the pathway of oxytocin delivery to CA2, we mapped oxytocinergic projections from the paraventricular nucleus (PVN), a primary oxytocin source (Cui et al., 2013; Mitre et al., 2016; Raggenbass et al., 1998). The PVN of *oxytocin-IRES-cre* mice (Irani et al., 2010; Wu et al., 2012) was injected with a Cre-dependent adeno-associated virus (AAV) encoding yellow fluorescent protein (YFP) fused to the excitatory opsin ChETA. YFP expression was confirmed in the PVN (Figure S1B2) and found in oxytocinergic fibers forming bouton-like puncta near CA2 somata (Figures S1C and S1D; Figure 1B). The oxytocinergic fiber density was enriched in areas CA2 and CA3 relative to CA1 (Figures S1C and S1D). Our data indicate that CA2 pyramidal cells both express OXTRs and receive oxytocinergic input, cueing study of OXTR function.

Activation of Oxytocinergic Outputs or OXTR Excites CA2 Pyramidal Neurons

Morphological and electrophysiological criteria (Chevaleyre and Siegelbaum, 2010; Dudek et al., 2016) distinguished CA2 pyramidal cells from those in the bordering area CA1 (Table

1). CA2 pyramidal cells had apical dendrites that bifurcated close to the soma (arrow, Figure 2A; Table 1), and the input resistance of pyramidal cells was lower in CA2 (81.4 ± 3.5 megaohms [MΩ]) than in CA1 (147.4 ± 8.9 MΩ), whereas cell capacitance was higher (262.7 ± 9.1 picofarads [pF] in CA2, 161.0 ± 6.6 pF in CA1; Table 1). As in prior work (Chevaleyre and Siegelbaum, 2010), CA2 pyramidal cells displayed delayed firing after depolarizing current steps and little voltage sag during hyperpolarizing current steps (Table 1; Figure 2B).

CA2 pyramidal neurons clearly responded to optogenetic stimulation of oxytocinergic fibers (Figure 1B1) following viral delivery of ChETA-YFP to the PVN of *oxytocin-IRES-Cre* animals (Figure S1B2). Exposure to blue light evoked a 6.25 ± 3.34 mV (mean ± SEM) depolarization (Figure 1C), accompanied by closely spaced groups of spikes (Figures 1D and 2G). Defined as 25 or more spikes in 5 s, bursts were evoked in 7 of 8 CA2 pyramidal cells within 20 min of light stimulation, but in 0 of 4 neurons pre-incubated with OTA (1 μM), a selective OXTR antagonist ($p < 0.02$, χ^2 test; Figure S2). Likewise, bursting activity was not evoked by light stimulation in the absence of viral ChETA expression (0 of 4 neurons; data not shown).

In complementary experiments, we exposed slices to the highly specific OXTR agonist [Thr^4,Gly^7]-oxytocin (TGOT, 400 nM), avoiding activation of vasopressin receptors. OXTR activation via TGOT depolarized 100% of CA2 pyramidal cells recorded in current clamp configuration (6.53 ± 1.03 mV, $n = 7$, $p < 0.005$; Figure 2C). In contrast, CA1 pyramidal cells displayed little or no direct depolarizing response (0.9 ± 0.4 mV, $n = 6$, $p > 0.2$) with synaptic transmission blocked. TGOT-induced depolarization in CA2 pyramidal cells was observed with and without glutamatergic and GABAergic blockade (Figure 2D), indicating that OXTR stimulation depolarizes the cells directly, not solely by altering synaptic inputs. Further experiments were carried out with glutamate receptors blocked (to avoid recurrent circuit excitation) but gamma-aminobutyric acid (GABA) receptors spared (to avoid complications of circuit disinhibition) unless specified otherwise. TGOT-induced depolarization in CA2 pyramids induced burst firing in 10 of 12 cases (Figures 2E–2G). The median TGOT-evoked firing frequency (~14 Hz) was close to that of light-driven spiking (~15 Hz; Figure 2G) and similar to firing rates in CA2 pyramidal cells *in vivo* (Kay et al., 2016).

OXTR Activation Promotes CA2 Pyramidal Cell Firing and Alters Spike Shape

We next studied the consequences of OXTR activation in CA2 pyramidal cells. TGOT caused reversible enhancement of excitability; depolarizing currents evoked higher firing rates during OXTR activation (Figure 3A). Similarly, less current was required to drive the cell to fire spikes at a given frequency (Figure 3B). This TGOT-induced leftward shift in the frequency-current (F-I) relation was quantified at 10 Hz and averaged 85.1 ± 20.2 pA (mean ± SD, $n = 5$, $p < 0.01$; Figure 4B). In contrast, exposure to arginine vasopressin (with ($d(CH_2)_5^1$,$Tyr(Me)^2$,Thr^4,Orn^8,des $Gly\text{-}NH_2^9$)-Vasotocin trifluoroacetate salt [OTA] to prevent crossover to OXTR) did not shift the F-I curve (Figure S3; $n = 5$, $p > 0.44$; Pagani et al., 2015). Thus, the enhancement of excitability produced by TGOT was a specific response to OXTR activation.

A potential mechanism for the OXTR-mediated depolarization is increased non-selective cation conductance with a consequential decrease in overall cell membrane resistance, as previously reported in hippocampal interneurons (Owen et al., 2013; Zaninetti and Raggenbass, 2000). In contrast, TGOT *increased* total input resistance (Figure 3C; 80.7 ±1.7 MΩ control, 112.9 ± 8.7 MΩ TGOT, n = 13, $p < 0.0001$). This suggested that OXTR activation might diminish a membrane conductance with a hyperpolarizing influence on the resting membrane potential, enhancing excitability (Figure 3A).

Additionally, action potentials generated during OXTR activation exhibited clear changes in configuration: an ~5-mV reduction in peak amplitude (80.0 ± 4.2 mV control, 74.9 ± 4.6 mV TGOT, $p < 0.005$, n = 7), whereas action potential duration remained unchanged (spike half-width, 1.19 ± 0.10 ms control, 1.19 ± 0.07 ms TGOT, $p > 0.9$, n = 6), and the after-hyperpolarization was attenuated (5.2 ± 1.5 mV control, 3.6 ±1.6 mVTGOT, n = 7, $p < 0.008$). These changes were evident in averaged spike waveforms (Figure 3D) and phase-plane plots (dV_m/dt versus V_m; Figure 3E), highlighting the briefest, most dynamic phases of the spike. Peak action potential and after-hyperpolarization amplitudes were strongly correlated (n = 30 spikes from 7 cells; $r = 0.76$, $p < 0.001$), even when control and TGOT conditions were taken together, as expected from activation of repolarizing currents near the spike peak (Figure 3F). In TGOT, the maximum in dV_m/dt, reflecting the peak inward excitatory current, was clearly diminished. In contrast, the threshold potential was not changed (Figure 3G; −41.0 ± 1.5 mV control, −40.2 ± 1.3 mVTGOT, n = 7, $p > 0.35$), a plausible dissociation given that the persistent sodium current (I_{NaP}) governing the spike threshold (Yamada-Hanff and Bean, 2015) is distinct from the inward current that dominates $(dV_m/dt)_{max}$.

Having found OXTR-induced changes in both excitability and spike shape, we asked whether these alterations occur in series or in parallel, a first step toward understanding the mechanism(s) of repetitive burst firing in CA2 pyramidal cells.

Excitability and Action Potential Shape Are Both Dependent on PLC Activity

OXTRs activate G-proteins that couple to downstream signal transduction pathways and, thus, trigger cellular events (Gimpl and Fahrenholz, 2001; Nishimori et al., 2008). Well-studied neuromodulators such as substance P (Takano et al., 1995) and acetylcholine (Brown and Yu, 2000) operate via PLC activation, suggesting that PLC might mediate OXTR effects. Indeed, pre-incubation of slices with a PLC blocker (U73122, 5 mM) abrogated the TGOT-induced increase in cell excitability, eliminating the F-I curve shift (Figure 4A–B; n = 5, $p > 0.2$, paired 2-tailed Student's t test). PLC activation can induce release of intracellular Ca^{2+}, but inclusion of a fast on-rate Ca^{2+} chelator ((1,2-bis(o-aminophenoxy)ethane-N,N,N′,N′-tetraacetic acid) [BAPTA], 20 mM) in the recording pipette had no effect on TGOT-induced excitability (Figure 4B; n = 6, $p > 0.65$, paired 2-tailed Student's t test).

Examination of the spike waveform revealed that PLC activity also mediated the OXTR-driven reduction in spike amplitude; no change was seen upon PLC block with U73122 (Figures 4C and 4D; n = 5, $p > 0.5$). However, the reduced spike amplitude was also prevented by intracellular BAPTA (Figures 4C and 4D; n = 6, $p > 0.07$). Thus, the spike height depended on the availability of intracellular Ca^{2+}, unlike the change in excitability.

These data reveal that the mechanisms altering cell excitability and action potential shape are largely dissociable downstream of a common requirement for PLC activation, prompting tests of how these OXTR-driven changes might be distinguished.

M-Current Regulation of Excitability but Not Action Potential Shape

Both the membrane depolarization (Figures 2C and 2D) and increased input resistance (Figure 3C) could be explained by a decrease in a basally active repolarizing conductance. "M-current" potassium channels are partly open near resting potential, regulated by G-protein coupled receptor (GPCR) signaling and often control somatic excitability and bursting (Bley and Tsien, 1990; Brown and Yu, 2000; Brown and Adams, 1980; Hernandez et al., 2008), making them a likely candidate. Neuronal M channels are hetero-tetramers with KCNQ2 and KCNQ3 subunits and require binding of phosphatidylinositol 4,5-bisphosphate (PIP_2) to all KCNQ3 subunits for maximum opening (Telezhkin et al., 2012). A well-studied mechanism of M-current modulation used by muscarinic agonists depends on PLC-dependent hydrolysis and depletion of PIP_2 from the membrane but not intracellular Ca^{2+} (Suh et al., 2004; Wang et al., 1998).

Immunostaining for KCNQ3 in the *stratum pyramidale* revealed a pattern of expression in CA2 pyramidal cells similar to OXTR (Figure S4), suggesting that OXTR signaling might modulate nearby M channels. To test this, we turned to pharmacological experiments using retigabine, an anticonvulsant agent that binds to KCNQ2, locking the M channel in an open conformation (Wuttke et al., 2005). Co-application of retigabine with TGOT reduced the OXTR-driven depolarization in a concentration-dependent manner; depolarization was partially reduced at 10 μM and completely blocked at 100 μM retigabine (Figure 4E; excitatory and inhibitory blockers present to exclude influence of synaptic input). Pre-incubation with retigabine (100 μM) caused slight hyperpolarization (1.34 ± 0.90 mV, mean ± SD, n = 4), suggesting that some M channels may be closed at rest.

To test whether M-current inhibition accounts for TGOT-mediated depolarization, we applied a KCNQ channel blocker, 10,10-bis(4-pyridinylmethyl)-9(10H)-anthracenone (XE991, 10 μM; Zaczek et al., 1998), that depolarized CA2 pyramidal cells (4.2 ± 0.5 mV, n = 6) and increased their excitability, causing a leftward shift in the F-I curve (Figure 4F; 70.4 ± 15.4 pA reduction in current needed to drive 10 Hz spiking, n = 5). Subsequent addition of TGOT failed to shift the F-I curve further than XE991 alone. Thus, XE991 largely occluded the effects of OXTR activation (Figure 4F; n = 5, $p > 0.11$, 2-tailed paired Student's t test).

Strikingly, M-current manipulations that blocked or occluded TGOT effects on excitability were ineffective in preventing or mimicking TGOT effects on action potential shape. For example, XE991 failed to reduce peak amplitude (−0.68% ± 1.97% change) or after-hyperpolarization amplitudes and also spared the ability of TGOT to alter spike amplitude (−7.27% ± 5.01% change, $p < 0.05$, Student's paired t test, n = 4; Figures 4G and 4H), suggesting a mechanism other than M-current modulation.

Modulation of Spike Shape but Not Excitability Is Mediated by PKC

PLC cleavage of PIP_2 generates the lipidic messenger diacylglycerol (DAG), which can activate PKC. PKC regulates voltage-gated sodium channels via direct phosphorylation

(Carr et al., 2003). In previous studies, muscarinic receptor activation of neuronal PKC decreased fast Na^+ currents (Cantrell et al., 1996), accelerated slow inactivation, and reduced channel availability (Carr et al., 2003; Chen et al., 2006). Thus, PKC signaling was a likely candidate for mediating OXTR effects on action potential configuration (Figures 5A–5E). Indeed, preincubation with the PKC blocker bisindolylmaleimide I (BIS, 10 μM) virtually eliminated OXTR effects on action potential shape. In the presence of BIS, TGOT application failed to reduce spike amplitude ($n = 6$, $p > 0.27$, paired two-tailed Student's t test) or after-hyperpolarization amplitude ($n = 6$, $p > 0.16$, unpaired two-tailed Student's t test) (Figures 5C–5E). In contrast, BIS pretreatment spared the enhancement of cell excitability following OXTR activation, leaving unchanged the TGOT-induced leftward shift of the F-I curve (Figures 5A and 5B, $n = 6$, $p > 0.3$), the TGOT-induced depolarization (BIS −66.9 ± 0.59 mV versus BIS+TGOT −62.7 ± 1.09 mV, $n = 6$), and the increase in input resistance (BIS 88.92 ± 6.30 MΩ versus BIS+TGOT 127.60 ± 16.65 MΩ, $n = 6$). The distinction between effects dependent and independent of PKC was further probed by direct activation of PKC with the DAG analog 1-oleoyl-2-acetyl-sn-glycerol (OAG, 20 μM), bypassing OXTRs. Reassuringly, OAG did not enhance excitability (Figure 5B; $n = 5$, $p > 0.8$) but did reduce the action potential amplitude compared with baseline (Figures 5C and 5D; $p < 0.007$). Taken together, these results show that, following OXTR activation, PKC activity drives changes in spike waveform but is not responsible for increased excitability.

We also investigated the role of PKC in slow changes in net excitatory currents in CA2 pyramidal cells, using cessation of spiking as a proxy. Slow inactivation of sodium conductance is a well-known gating mechanism that depends on neuronal activity, takes seconds to develop, and, in turn, shapes repetitive firing (Carr et al., 2003). Repetitive injections of depolarizing current (3 s long, 0.3 Hz) were applied to CA2 pyramidal cells to mimic the intermittent bursting patterns seen during OXTR activation (Figure S5). Failure of neuronal spiking during the prolonged current injection was hastened by OAG (Figures 5F, S5A, and S5B), and the spike threshold increased gradually (Figure S5C), suggesting that PKC may accelerate depolarization-dependent reductions in Na^+ channel availability in CA2 pyramidal cells, as in neocortical neurons (Carr et al., 2003).

So far, our experiments indicate that OXTRs use divergent branches of the GPCR-coupled PLC pathway to bring about electrophysiological changes (Figure 5G). PLC activation drives the degradation of PIP_2 and the consequent deactivation of M channels when PIP_2 dissociates from KCNQ3 subunits (Hernandez et al., 2008). Reduction of the M-current accounts for the steady depolarization, increased membrane resistance, and enhanced excitability. In another signaling branch, sequelae of PIP_2 degradation (DAG and, possibly, elevated intracellular Ca^{2+}) activate PKC and, thus, downregulate the net excitatory current (Carr et al., 2003). As spike overshoot is reduced, repolarizing K^+ channels are less strongly activated, and undershoot is decreased. The signaling branches are clearly divergent, at least with regard to basic features of single spikes.

M Channel Inhibition and PKC Modulation of Excitatory Current Are Necessary and Sufficient for OXTR Effects on Burst Firing

Having defined distinct outcomes of the two branches of OXTR-driven signaling, we next asked whether those outcomes might re-converge to support the overall pattern of repetitive firing. The TGOT-induced bursts of action potentials in CA2 pyramidal cells (Figures 2E–2G and 6A) had mean burst durations of 2.75 ± 0.40 s and a mean intraburst frequency of 33.5 ± 2.6 Hz (Figures 6B and 6C). Similar firing patterns of CA2 neurons have been observed during immobility and sleep in the rat (Kay et al., 2016), suggesting that a basic understanding of CA2 burst firing may be relevant to hippocampal circuits *in vivo.* To clarify the basis of bursting, we separately examined the effects of M-current inhibition and PKC activation. Like TGOT, application of the KCNQ channel blocker XE991 drove cell depolarization and spike bursts (Figure 6A). However, compared with bursts driven by TGOT, XE991-induced bursts lasted longer (5.14 ± 0.19 s, $p < 0.001$; Figure 6B) and reached a lower intraburst frequency (9.64 ± 0.66 Hz, $p < 0.001$; data from 137 bursts and 3 cells; Figure 6C). Similar results were obtained by application of TGOT in combination with the PKC blocker BIS (Figure 6A, bottom right); again, bursts were longer in duration (4.63 ± 0.53 s; Figure 6B) and lower in intraburst frequency (16.9 ± 2.6 Hz, n = 112 bursts, 3 cells; Figure 6C) than with TGOT alone. Finally, we attempted to reconstitute the multiple branches of OXTR-driven signaling by combined application of the M-current inhibitor XE991 and the PKC activator OAG (bottom left trace, Figure 6A; rightmost bars, Figures 6B, 6C, and 6E). In this case, the CA2 neurons produced bursts close in both duration (1.7 ± 0.1 s) and intraburst frequency (26.4 ± 2.1 Hz, n = 103 bursts, N = 3 cells) to bursts with TGOT itself (all differences not significant).

These results underscore the importance of the two branches of OXTR-mediated signaling, working in coordination. PKC activity, presumably promoting phosphorylation and modulation of voltage-gated Na^+ channels (Carr et al., 2003), proved essential for shaping both the frequency and duration of the bursts. The interspike interval (ISI) of the initial action potentials in a burst was shortest when PKC was activated by TGOT or OAG; the ISI was more than 5-fold longer when PKC activation was absent (XE991 alone) or blocked (TGOT+BIS) (Figures 6D and 6E, $p < 0.001$). One interpretation is that PKC phosphorylation reduces net inward excitatory current and spike height, allowing less repolarizing K^+ current to be activated and permitting faster triggering of the subsequent spike (Figures 6A–6C). Burst duration is also affected by PKC-mediated modulation of excitatory current, as seen in OAG effects on directly evoked bursts (Figures 5F and S5).

CA2 Fast-Spiking Interneurons Are Modulated by TGOT and Help Shape Pyramidal Cell Bursting

Finding cooperation between multiple signaling branches leaves open whether the bursting patterns arise cell-autonomously or require interactions at the circuit level. In fact, fast-spiking, parvalbumin-positive (PV+) interneurons in hippocampal CA1 are strongly modulated by TGOT (Owen et al., 2013), raising the issues of whether OXTR stimulation affects CA2 fast-spiking interneurons and how this might influence CA2 pyramidal cell firing. PV+ interneurons in area CA2 are of particular interest in schizophrenia (Discussion).

Co-staining of CA2 for OXTR and PV indicated that PV+ interneurons express OXTR and confirmed the greater abundance of PV+ cells in CA2 than CA1 or CA3 (Figure 7A). Across the hippocampal subregions, the proportion of PV+ neurons that were also OXTR+ was 70.5% (n = 44). We next performed whole-cell current clamp recordings from putative PV+ interneurons in the CA2 *stratum oriens* and *stratum pyramidale,* identified by their fluorescence (PV-Cre, transgenic reporter line Ai9) and their fast-spiking response to depolarizing current pulses (Figure 7B, inset). In line with our previous findings in CA1 (Owen et al., 2013), TGOT significantly depolarized fast-spiking interneurons in CA2 (Figure 7B; $\Delta = 15.45 \pm 0.8$ mV, n = 4, $p < 0.0003$ without blockers present, Student's t test). This depolarization was largely blocked by pre-incubation with 100 mM retigabine (Figure 7B; $\Delta = 1.93 \pm 0.7$ mV) and seen even with glutamatergic blockers present ($\Delta = 5.06$ 0.08 mV, n = 7, $p < 0.004$; 2,3-Dioxo-6-nitro-1,2,3,4-tetrahydrobenzo[f] quinoxaline-7-sulfonamide [NBQX] and 5-Phosphono-DL-nor-valine, DL-2-Amino-5-phosphonovaleric acid [APV]). Excitability was enhanced, as reflected by a leftward shift of the F-I curve in the presence of the excitatory blockers (Figure 7C), again suggesting a direct effect of TGOT. The underlying mechanism in CA2 PV+ neurons appeared similar to that in excitatory neurons; the input resistance of CA2 PV+ interneurons increased with a similar time course as that of CA2 pyramidal cells (Figure S6C; $\Delta = 19.1 \pm 6.5$ MΩ, n = 9, $p < 0.02$, paired 2-tailed Student's t test). The shift of the F-I curve required PLC action but not activity of PKC (Figures S6A and S6B); PV+ cells expressed KCNQ3 subunits and depolarized in response to XE991 (data not shown).

These findings in CA2 PV+ neurons prompted us to reexamine PV+ interneurons in CA1 and a possible role of the M-current. Indeed, PV+ interneurons in CA1 showed increased input resistance in response to TGOT (Figure S6F), similar to that of CA2 neurons (Figure S6C). Also consistent with OXTR-mediated inhibition of the M-current, TGOT depolarized CA1 PV+ interneurons (peak $\Delta = 10.0 \pm 0.7$ mV, n = 6, $p < 0.0001$, 1-way Student's t test). Again, the M-current activator retigabine blunted TGOT-induced depolarization, reducing it by ~70% (peak $\Delta = 3.4 \pm 1.1$ mV retigabine, 10.0 ± 0.7 mV control; Figure S6F). The residual ~30% depolarization could reflect a contribution of enhanced non-selective cation current (Owen et al., 2013; Zaninetti and Raggenbass, 2000), previously studied with Cs+ in the recording pipette. However, with K+ rather than Cs+ as the main cytoplasmic cation, modulation of the M-current appears to be the major mechanism of OXTR-driven depolarization.

Having established that OXT neuromodulation affects both excitatory and inhibitory cells within CA2, we looked for clues that the two populations interact with one another, as previously seen in direct paired recordings (Mercer et al., 2012). Recording from CA2 fast-spiking interneurons revealed enhancement of excitatory postsynaptic potentials (EPSPs) during TGOT application (Figure 7D), both in frequency (14.3 ± 1.2 Hz baseline, 24.9 ± 1.1 Hz TGOT, n = 5, $p < 0.05$, paired 2-tailed Student's t test) and amplitude (0.7 ± 0.03 mV baseline, 1.1 ± 0.2 mV TGOT, n = 5, $p < 0.03$, paired 2-tailed Student's t test). The TGOT-driven increase in EPSP frequency was greatly lowered by blocking glutamate receptors with NBQX and APV (2.0 ± 1.1 Hz, n = 6, $p < 0.001$, unpaired 2-tailed Student's t test) or by eliminating action potentials with tetrodotoxin (TTX) (7.5 ± 0.5 Hz, n = 4, $p < 0.001$, unpaired 2-tailed Student's t test) (Figure 7D), consistent with the excitatory drive from

pyramidal neurons of CA2 (or, conceivably, CA3). Conversely, voltage-clamp recording from CA2 pyramidal cells with glutamate receptors blocked (NBQX and APV) uncovered a TGOT-driven increase in inhibitory event frequency (Figure 7E, 15.2 ± 1.6 Hz baseline, 19.3 ± 2.0 Hz TGOT, n = 7, $p < 0.001$) and IPSC amplitude (9.7 ± 0.8 pA baseline, 11.3 ± 1.2 pA TGOT, n = 7, $p < 0.04$, paired 2-tailed Student's t test). Thus, OXTR-induced enhancement of inhibition onto CA2 pyramidal cells would be expected to counteract TGOT-driven membrane depolarization. Such a braking effect was already evident from the enlargement of TGOT-driven membrane depolarization in CA2 pyramidal neurons by gabazine (Figure 2D).

These findings heighten interest in the interplay between excitatory and inhibitory neurons during burst firing in CA2. The burst patterns in CA2 pyramidal cells in the absence and presence of gabazine revealed clear effects of inhibition (Figure 7F). The GABAergic input significantly elevated the intraburst frequency (27.2 ± 5.6 Hz TGOT only, 11.2 ± 2.0 Hz TGOT+gabazine) and restricted burst duration (1.9 ± 0.5 s TGOT only, 4.8 ± 1.1 s TGOT +gabazine). These more than 2-fold effects may be attributed to the role of GABAergic inhibition in the promotion of rapid repetitive firing in pyramidal cells (Cardin et al., 2009). Phasic increases in GABA receptor chloride conductance will pull the membrane potential toward chloride reversal potential (E_{Cl}), hastening both spike repolarization and inter-event depolarization.

No Effect of OXTR Activation on CA2 Presynaptic Inputs onto CA1 Pyramidal Cells

To test whether OXTR stimulation alters presynaptic output of CA2 onto its major downstream target, hippocampal area CA1, we injected a Cre-dependent AAV encoding tdTomato and channelrhodopsin-2 (ChR2) into both dorsal hippocampi of *Amigo2* transgenic mice expressing Cre recombinase in CA2 pyramidal cells (Hitti and Siegelbaum, 2014). Expression of ChR2 in CA2 pyramidal cells was confirmed by expression of tdTomato (Figure 8A) and blue light stimulation of CA2 spiking (Figure S7A). CA1 pyramidal cells did not express ChR2 or fire action potentials in response to blue light stimulation (Figures 8A and S7A). However, blue light stimulation did drive EPSCs in CA1 pyramidal cells (Figure 8B), consistent with the direct excitatory connection between CA2 and CA1 pyramidal cells (Dudek et al., 2016). The main CA2 output primarily targeted the *stratum oriens* of CA1 (Figure 8A), as expected from previous anatomical studies (Lorente De Nó, 1934; Shinoharaet al., 2012; Tamamaki et al., 1988). Although evidence suggests that excitatory CA2 axons connect more strongly to deep CA1 pyramidal cells than to superficial ones (Kohara et al., 2014), all CA1 pyramidal cells we recorded from, without preference for one subtype or another, displayed EPSCs in response to blue light.

To test whether OXTR activation altered the probability of transmitter release, we evoked EPSCs with a 1-s, 10-Hz stimulation train at a low blue light intensity (0.5-ms pulse width, stimulation strength adjusted to elicit a measurable EPSC in ~20% of stimulus trials). TGOT produced no clear increase in evoked EPSC likelihood (Figure 8B; 20.5% ± 13.0% baseline, 26.7% ± 11.0% TGOT, n = 7, $p > 0.12$). With stronger blue light stimulation to elicit EPSCs in 100% of trials, TGOT also failed to increase the overall evoked excitatory charge transfer

(Figure 8B; 2.5 ± 0.5 picocoulombs [pC] baseline, 2.2 ± 0.5 pC, n = 7, p > 0.17). Finally, paired-pulse ratios remained unchanged upon exposure to TGOT (Figure 8C; n = 7, p > 0.9).

We did, however, detect an increased incidence of spontaneous EPSCs onto CA1 pyramidal cells during TGOT application, reflected by a halving of the inter-event interval (IEI) (Figure 8D; 362.8 ± 54.1 ms baseline, 172.7 ± 35.9 ms TGOT, n = 8, p < 0.007, paired 2-tailed Student's t test). This could be due to increased firing of CA2 neurons directly influenced by TGOT, although a contribution from CA3 pyramidal cells was not excluded; TGOT also increased excitatory synaptic inputs onto CA2 pyramidal cells (Figure S8). Notably, the relative decrease in IEI between spontaneous EPSCs with TGOT present was greater onto CA1 pyramidal cells closer to the CA2 border (Figure 8E, Pearson r = 0.78, p < 0.03, n = 8). This proximity dependence makes sense if TGOT acted on upstream neurons rather than their nerve terminals; the number of connected upstream neurons falls off with distance because hippocampal slices imperfectly match the laminar axon distribution (Tamamaki et al., 1988). Taken together, our evidence weighs against a direct action of OXTRs at presynaptic boutons of CA2 axons and in favor of an effect at or near cell bodies of upstream pyramidal neurons on the other side of the CA1-CA2 border.

CA2 Firing Patterns Govern the Excitatory:Inhibitory Ratio and Short-Term Plasticity of CA2→CA1 Inputs

Even if OXTR activation has little direct influence on presynaptic terminals of CA2 axons, their pattern of firing could still exert profound effects on the dynamics of presynaptic release. Bursts of action potentials interspersed with periods of rest are commonly observed in neuronal systems and can increase the reliability of synaptic communication (Lisman, 1997). We therefore tested how variations in burst duration and intraburst frequency shape CA2 output onto CA1 pyramidal cells by interposing a pause (1 s) between two high-frequency (30-Hz) bursts of blue light stimulation of CA2 pyramidal cells. The stimulus parameters were modeled after OXTR-driven bursts (mean intraburst frequency with TGOT, 33.5 ± 2.6 Hz; Figure 6C). We compared the synaptic efficacy of this burst-pause-burst pattern with that of continuous stimulation with the same number of light pulses over the same total elapsed time (achieved with steady stimulation at 25.7 Hz). We isolated EPSCs by voltage-clamp recording at the reversal potential for GABAergic Cl^- currents and compared the cumulative charge for both stimulation paradigms (Figure 8F). Interposing a pause in the light stimulation increased the charge transfer by 26.6% over the continuous stimulation paradigm, a modest but statistically significant effect (Figure 8G; n = 7, p < 0.01, paired 2-tailed Student's t test).

We also considered the effect of burst frequency on disynaptic inhibition arising from CA2 drive of CA1 feedforward inhibition. Short-term plasticity of co-activated excitatory and inhibitory inputs modifies the balance between excitation and inhibition, acting as a gain control mechanism (Heiss et al., 2008; Klyachko and Stevens, 2006). We probed the CA2→CA1 circuitry for potential short-term plasticity of excitatory and inhibitory inputs during high frequency stimulation (STAR Methods). Both excitatory and inhibitory synaptic outputs displayed synaptic depression, but IPSC depression was consistently greater than that of EPSCs during both 10- and 30-Hz blue light stimulation (Figure 8H). Thus, high-

frequency firing, as occurs during a TGOT-induced burst, disproportionately accelerates synaptic depression of inhibitory currents. As a result, the IPSC:EPSC ratio shifts against inhibition, increasing the net excitatory drive (Figure 8I). The reduction in the I:E ratio was significantly greater during 30-Hz stimulation, falling to 18.3% ± 7.5% of baseline as opposed to 45.0% ± 5.9% at 10 Hz ($n = 9$, $p < 0.02$, unpaired 2-tailed Student's t test), suggesting that OXTR-induced high-frequency bursts would greatly affect the net drive CA2 exerts on CA1 circuits by enhancing excitation relative to inhibition.

DISCUSSION

The patterns of expression of OXTRs and oxytocinergic fibers support the intuition that oxytocin, long considered a "social Peptide" (Insel, 2010; Nishimori et al., 2008), would affect hippocampal area CA2, an understudied region (Dudek et al., 2016; Jones and McHugh, 2011) strongly implicated in social behavior (Hitti and Siegelbaum, 2014; Raam et al., 2017; Lin et al., 2018). Indeed, we uncovered a powerful effect of OXTRs on repetitive firing in CA2 and showed how the bursts arose from diverse signaling events, ionic mechanisms, and circuit actions operating in concert. In CA2, pyramidal neurons as well as PV+ interneurons were directly and independently responsive to the OXTR-selective agonist TGOT. In consistently depolarizing CA2 pyramidal cells, TGOT overcame the neurons' hyperpolarized resting potential (Chevaleyre and Siegelbaum, 2010) and greatly enhanced excitability. In contrast, CA1 pyramidal cells were not directly affected by TGOT (Owen et al., 2013). Nevertheless, CA1 pyramidal neurons are positioned to receive a powerful OXTR-driven input from CA2; indeed, the bursting patterns in CA2→CA1 axons strongly tilted the E:I ratio in favor of excitation. Thus, the regional specificity of oxytocin action on principal neurons still allows widespread modulation of hippocampal information processing.

Bursting in CA2 Excitatory Neurons: Coordinated Signaling Driven by OXTR-Dependent PIP_2 Hydrolysis

The TGOT-driven increase in excitability in CA2 pyramidal cells was tied to *increased* input resistance (R_{in}), not anticipated from previous studies in rat CA1 inhibitory neurons that focused on enhancement of non-selective cation conductance (Owen et al., 2013; Raggenbass et al., 1998). In CA2 pyramidal cells, depolarization and increased Rin resulted from PLC-dependent closure of KCNQ K^+ channels (M-current) based on the following findings: TGOT-driven depolarization was prevented by inhibition of PLC; CA2 pyramids express KCNQ3, the PIP_2-binding component of M channels; the M-current enhancer retigabine prevents TGOT-driven depolarization; and the KCNQ-specific blocker XE991 mimics and occludes TGOT effects on excitability.

Although PIP2 hydrolysis and modulation of KCNQ channels were necessary to explain TGOT-driven bursting, these events were not sufficient. The tightly linked reductions in spike and after-hyperpolarization amplitudes were shown to arise from other outcomes of PLC-mediated PIP2 breakdown, involving DAG- and, likely, Ca^{2+}-dependent activation of PKC. The effects on spike height and undershoot depth were mimicked by OAG and prevented by BIS block of PKC or by buffering of $[Ca^{2+}]_i$. Such effects were seen even with

TGOT-induced membrane depolarization occluded with XE991 and, thus, resulted from modulation of peak inward excitatory current rather than an indirect effect of membrane depolarization on its availability. Our findings align with previous reports that PKC-mediated phosphorylation reduces peak conductance and promotes slow inactivation of Na^+ channels (Cantrell and Catterall, 2001; but see Chen et al., 2006). Lowering the spike overshoot should lessen activation of voltage-gated K^+ channels, attenuate the post-spike undershoot, and favor rapid transition to the next spike. In turn, rapid firing will favor PKC-dependent acceleration of slow Na^+ channel inactivation and earlier termination of bursts. This scenario does not exclude indirect changes in other conductances not directly controlled by PIP_2 breakdown. It will be interesting to compare the signaling mechanisms described here with those of other neuromodulators such as acetylcholine. Muscarinic inputs operate via GPCR-driven PIP_2 breakdown, famously inhibit M-current, and drive PKC-mediated changes in spiking (Cantrell et al., 1996; Carr et al., 2003). Modulation of K^+ and Na^+ currents by muscarinic acetylcholine receptor (mAChR) agonists causes isolated excitatory neuronal somata to generate bursting (Golomb et al., 2006), suggesting a similar coordination of multiple signaling branches, although this remains incompletely tested.

Along with modifications of pyramidal cell-intrinsic properties, GABAergic inhibition, possibly from co-activated PV+ interneurons, was also important for shaping TGOT-induced bursts. Without GABAergic input, the bursts were more than 2-fold longer and less intense. This showed that full-blown oxytocinergic modulation of CA2 firing requires multiple signaling events in multiple modulator-responsive cell types.

Implications for OXT Modulation of Circuit Function and Behavior

The cellular mechanisms of OXTR modulation are well-suited to sculpt the operation of hippocampal circuits *in vivo.* By shutting off the M-current in CA2 pyramidal neurons, socially driven oxytocinergic input would counteract their basally negative resting potential (Chevaleyre and Siegelbaum, 2010) and boost the remapping of CA2 place fields induced by social stimuli (Alexander et al., 2016). Additionally, OXTR stimulation of CA2 inhibitory neuron firing might dampen the initially strong GABAergic transmission in CA2 (Piskorowski and Chevaleyre, 2013) via activity-dependent synaptic depression (Figure 8H; Owen et al., 2013; Marlin et al., 2015; Oettl et al., 2016). In either case, OXTR signaling would promote depolarization of CA2 pyramids and long-term potentiation (LTP) of CA3-CA2 neurotransmission (Lin et al., 2018; see also Mitre et al., 2016; Pagani et al., 2015). In these ways, oxytocin effects at the cellular level could help engage plasticity mechanisms to influence CA2 representation of space (Alexander et al., 2016) and, in turn, hippocampal-dependent spatial memory, long known to be influenced by oxytocin (Tomizawa et al., 2003). As a possible example, recent *in vivo* recordings in rodents have identified CA1 pyramidal cells whose place fields represent nest position (Kay et al., 2016; Lin et al., 2007). Perhaps OXTR-promoted CA2 firing triggers plasticity in CA1 place cells for encoding nest location.

Social memory (recollection of a familiar conspecific) is another likely target of oxytocin modulation of CA2 neurons, given that social memory is impaired by genetic silencing of CA2 neuron output (Hitti and Siegelbaum, 2014) and targeted deletion of OXTRs in CA2

and CA3a excitatory neurons (Lin et al., 2018; Raam et al., 2017; see also Takayanagi et al., 2005). Our results provide ways of tying these observations together. Finding that OXTR stimulation specifically and strongly affects firing of such neurons links the behavioral deficits in OXTR knockout (KO) (Lin et al., 2018; Raam et al., 2017) and CA2 output-silenced mice (Hitti and Siegelbaum, 2014). Demonstration of severe frequency-dependent depression of feedforward inhibition from CA2 to CA1 suggests how high-frequency firing of CA2 pyramidal cells might elevate the net strength of their output onto CA1. Finally, CA2 neurons likely receive excitatory input from OXTR-bearing CA3 neurons, supplementing the direct effects of CA2 OXTR stimulation studied here.

Disease Pathology and Oxytocin in CA2

Schizophrenia is associated with impaired social behavior (Penn et al., 2008) and pathological changes in area CA2 (Benes et al., 2008). Studies report loss of PV+ interneurons, which are more abundant than in CA1 or CA3 (Botcher et al., 2014). In a mouse model of schizophrenia, heterozygous reeler mice, PV+ interneurons are less numerous (Nullmeier et al., 2011), and OXTR mRNA in CA2 is decreased (Liu et al., 2005). In the 22q11.2 microdeletion mouse, another schizophrenia model, PV+ interneurons are lost during development, inhibitory tone is reduced, and CA2 pyramidal cells undergo compensatory hyperpolarization (Piskorowski et al., 2016), paralleling elevated KCNQ2 in schizophrenic patients (Benes et al., 2008). Oxytocinergic stimulation could stimulate inhibitory neurons to restore inhibitory tone and counteract the pathologically hyperpolarized membrane potential of pyramidal cells. In this context, the multipronged effects of OXTRs might be well-suited to beneficially retuning circuit function.

STAR⋆METHODS

CONTACT FOR REAGENT AND RESOURCE SHARING

Further information and requests for resources and reagents should be directed to and will be fulfilled by the Lead Contact, Dr. Richard Tsien (richard.tsien@nyumc.org).

The OXTR-Cre mouse line was provided to us by Dr. Katsuhiko Nishimori (Tohoku University) in accordance with a Material Transfer Agreement between New York University and Tohoku University. If interested in the transgenic line, please contact Dr. Nishimori directly (knishimori@m.tohoku.ac.jp).

EXPERIMENTAL MODEL AND SUBJECT DETAILS

All procedures involving animals were approved by the Institutional Animal Care and Use Committee at the New York University Langone Medical Center, and in accordance with guidelines from the US National Institutes of Health. Animals were housed in fully equipped facilities in either the Alexandria Center for Life Science (New York City) or the NYU School of Medicine Science Building (New York City). The facilities were operated by Mispro Biotech Services Corporation and the Division of Comparative Medicine (DCM, NYU), respectively. Unless otherwise indicated, male mice, aged 2 – 3 months, were used for all experiments to avoid variation in OXTR expression throughout the estrous cycle of female mice (Nakajima et al., 2014). C57BL/6 mice (Jackson Labs; Stock No. 000664) were

used in wild-type experiments; homozygous *Oxytocin-ires-Cre* (Jackson Labs; Stock No. 024234) and hemizygote *Amigo2-Cre* mice (Jackson Labs; Stock No. 030215) were used for optogenetic studies. *OXTR-ires-Cre* mice were provided by Dr. Katsuhiko Nishimori (Tohoku University). *Ai14* mice (Jackson Labs; Stock No. 007908) were crossed *OXTR-ires-Cre* animals; their offspring were used in imaging experiments. In some experiments, PV-expressing interneurons were identified using a transgenic reporter. In these experiments, offspring of a cross between PV-Cre mice (Jackson Labs; Stock No. 008069) and Ai9 mice (Jackson Labs; Stock No. 007909) were used.

METHOD DETAILS

Viral Injections—For all viral injections, 2–3 month old mice were anesthetized with isofluorane (2%–5%) and placed in a stereotaxic apparatus (Kopf). Burr holes or craniotomies were made over targeted brain regions to permit pipette insertion. The pipettes (Drummond Scientific) were formed using a P-2000 laser puller (Sutter Instrument) to have a long tapered, 10–20 μm diameter tips. Pipettes were back-filled with mineral oil (Fisher Scientific) and then loaded with virus using a Nanoject II (Drummond Scientific). For identification of oxytocinergic inputs to the hippocampus, pAAV5-EF1α-DIO-ChETA-eYFP (1–1.2 μl; Penn Vector) was injected (0.1 μl/min) unilaterally into the PVN (from bregma in mm: 0.7 posterior, 0.25 lateral, 4 ventral) of *Oxt*-IRES-cre mice (from D. Olson and B. Lowell). For optogenetic manipulation of CA2 pyramidal cells, pAAV-EF1α-dflox.hChR2(H134R)-mCherry-WPRE-hGH (350 nl; Penn Vector) was injected (0.2 μl/min) bilaterally into CA2 (from bregma in mm: 1.6 posterior, ±1.6 medial/lateral, 1.7 ventral) of *Amigo2-cre* animals. After injection, the pipette remained in place for 5 min and was then slowly retracted. The scalp was then sutured shut, saline was administered subcutaneously, and buprenorphine (0.1 mg/kg) was administered subcutaneously for analgesia. Animals were allowed at least two weeks to recover to allow adequate expression of the virus.

Electrophysiology recordings—Mice 2–3 months old were anesthetized with a mixture of ketamine/xylazine (150 mg/kg and 10 mg/kg, respectively) and perfused transcardially with a ice cold sucrose solution containing (in mM): 206 Sucrose, 11 D-Glucose, 2.5 KCl, 1 NaH2PO4, 10 MgCl2, 2 CaCl2 and 26 NaHCO3. Following perfusion and decapitation, brains were removed and placed in the cold sucrose for sectioning before gluing to the stage of a Leica VT 1000S Vibratome. Transverse, 350 μm sections of left and right hippocampi were cut and transferred to an oxygenated, 34°C recovery chamber filled with artificial cerebro-spinal fluid (ACSF) containing (in mM): 122 NaCl, 3 KCl, 10 D-Glucose, 1.25 NaH2PO4, 2 CaCl2, 1.3 MgCl2, and 26 NaHCO3. Slices were allowed to recover for 1 h at 34°C and were then maintained at room temperature in oxygenated ACSF for 1–6 h before recording.

Hippocampal slice recordings were performed in a submerged chamber maintained at 32–34°C with a constant bath perfusion of ACSF (with or without pharmacological agents) at ~4 mL/min. Slices equilibrated in the chamber for >10 minutes before recording. Whole cell and cell-attached recordings were made with borosilicate glass pipettes pulled on a Sutter Instrument P-97 micropipette puller. Tip resistance ranged between 2–5 MΩ following fire polishing to enhance seal quality. For current clamp recordings, the intracellular solution

contained (in mM): 130 K-Gluconate, 1 $MgCl_2$, 10 HEPES, 0.3 EGTA, 10 Tris-Phosphocreatine, 4 Mg-ATP, and 0.3 Na-GTP. For voltage clamp recordings of spontaneous and evoked EPSCs, the intracellular solution contained (in mM): 130 $CsMeSO_3$, 6 CsCl, 1 $MgCl_2$, 10 HEPES, 0.3 EGTA, 10 Tris-Phosphocreatine, 4 Mg-ATP and 0.3 Na-GTP. Spontaneous IPSCs onto pyramidal cells were recorded in voltage clamp using a high Cl^- internal solution containing (in mM): 70 $CsMeSO_3$, 35 CsCl, 15 TEA-Cl, 1 $MgCl_2$, 0.2 $CaCl_2$, 10 HEPES, 0.3 EGTA, 10 Tris-Phosphocreatine, 4 Mg-ATP and 0.3 Na-GTP. Biocytin (0.1%) was including in the internal solution for morphological analysis of recorded cells.

Hippocampal regions and layers were identified visually with an upright microscope (Zeiss Axioskop 2 FS Plus) using infrared differential interference contrast (IR-DIC) optics. CA1 pyramidal cells and interneurons in the stratum pyramidale and oriens were often visualized while patching; CA2 pyramidal cells were patched without visual identification of the cell surface due to reduced tissue clarity. Recordings were made using a MultiClamp 700B amplifier (Axon Instruments, Union City, CA). Signals were filtered at 10 kHz using a Bessel filter and digitized at 20kHz with a Digidata 1322A analog-digital interface (Axon Instruments). Series resistance was monitored during recordings and maintained at < 25 MΩ.

To measure membrane depolarization and spontaneous burst firing, cells were held near resting potential under current clamp. When applied, pharmacological blockers were washed on 3–5 min prior to initiation of TGOT wash. For F-I curves, pyramidal cells were held undercurrent clamp to maintain a membrane potential near −70 mV, and 500 ms depolarizing and hyperpolarizing current injections were made in 10 or 20 pA increments. All data is a mean of at least 3 applied current injections. Membrane resistance was monitored throughout recordings via brief hyperpolarizing current pulses.

ChR2 experiments were performed > 2 weeks after AAV injection to allow for virus expression. Slices were cut as previously described and successful virus expression was verified by visualizing tdTomato in CA2 and the stratum oriens of CA1. Photostimulation of ChR2 was achieved through 470 nm light delivered to the slice field through a 40x objective. Illumination intensity was adjusted between 0.1–2.0 mW, depending on the experimental objective.

Immunohistochemistry

Animals were perfused with PBS followed by 4% paraformaldehyde in PBS. Whole brains were dissected and fixed overnight in 4% PFA, and then sucrose-protected overnight in 30% sucrose in PBS before embedding and freezing in optimal cutting temperature compound (Tissue-Tek O.C.T.) for sectioning. Frozen sections were cut on a cryostat at 16 μm and collected on HistoBond coated slides (VWR) for staining. Sections were blocked for 2–3 hours at room temperature in 0.2% Triton X-100 and 5% normal serum, then incubated at 4°C in the following primary antibodies for 12–20 hours: mouse anti-PV (Swant Cat# PV 25, RRID: AB_10000344, 1:500), rabbit anti-K_v7.3 (KCNQ3; Alomone Cat# APC-051, RRID: AB_2040103, 1:200), mouse anti-RGS14 (Neuromab, 1:100) and rabbit anti-OXTR (Mariela Mitre, Moses V. Chao, Robert C. Froemke, NYU School of Medicine Cat# OXTR-2 antibody RRID:AB_2571555, unpurified, 1:30). Sections were rinsed and then

incubated in species-appropriate Alexa Fluor conjugated secondary antibodies (Molecular Probes, 1:500) for 2–3 hours, and finally mounted with ProLong Gold Antifade Mountant with or without DAPI (ThermoFisher Scientific). Primary antibodies were omitted from some sections to serve as a control for antibody specificity. Fluorescent images were acquired on a Zeiss LSM 510 meta Imager.M1 confocal microscope.

For analysis of neuron morphology, pyramidal cells were held in whole cell configuration with a pipette containing 0.1% biocytin for > 15 min before being transferred to a 4% paraformaldehyde fixative solution for 12–24 h. Slices were rinsed and stained with a streptavidin Alexa Fluor 488 conjugate (Molecular Probes, Eugene, Oregon). Fluorescent mages were acquired on a Zeiss LSM 510 meta Imager.M1 confocal microscope, and maximum intensity projections of z stacks were generated in ImageJ (NIH). Neuron tracing was done manually (Wacom Intuos tablet).

QUANTIFICATION AND STATISTICAL ANALYSIS

Quantification of oxytocin fibers—Oxytocinergic inputs to the hippocampus were quantified by examining cre-dependent expression of eYFP from adult female *Oxt*-IRES-cre mice in a 200×200×12 μm volume of tissue, imaged at 63x. eYFP fibers and puncta were traced (ImageJ) by an observer blinded to hippocampal region, and fiber density (length per mm^2) was quantified.

Analysis of whole cell recordings—Current clamp recordings were analyzed offline using custom written routines in MATLAB (Mathworks) for membrane voltage, firing rate and action potential waveform analysis. Membrane resistance was monitored throughout recordings via brief hyperpolarizing current pulses. Spontaneous PSCs were detected offline using pClamp software for event detection.

Evoked post-synaptic events were recorded under voltage clamp at two holding potentials (V_1 *and* V_2) away from the known Cl^- reversal potential (E_{cl}). It was assumed that the excitatory and inhibitory conductances at V_1 were proportional to those at V_2, scaled by the ratio of driving forces at the two holding potentials. For each of the recorded currents (I_1 *and* I_2), fast-decaying excitatory component (Ex_1 *and* Ex_2) were isolated from slow-decaying inhibitory component (In_1 *and* In_2) using the following equations:

$$I_1 = Ex_1 + In_1$$
$$I_2 = Ex_2 + In_2$$

$$Ex_1 = Ex_2 V_1 / V_2$$
$$In_1 = In_2 \left(V_1 - E_{cl}\right) / \left(V_2 - E_{cl}\right)$$

Short-term depression of isolated excitatory and inhibitory conductance were calculated by normalizing to the amplitude of the first response in the stimulation train.

STATISTICAL ANALYSIS

Student's t test was used for comparisons between two groups. One- or two-way analysis of variance (ANOVA) was used for analysis between three or more groups. To compare the proportion of responsive cells following optogenetic stimulation of oxytocinergic fibers, with and without the antagonist present (Figure 1 and S1), we used a chi-square test. For determination of F-I curve shifts, the current required to drive the cell to fire at 10 Hz was interpolated from polynomial curves. Statistical analyses were performed using Prism 6.0 GraphPad and MATLAB (MathWorks). The statistical test used, the consequent p value and the number of cells that went into the calculation (n) are reported in the main text describing each figure. All quantifications are the result of data from at least 3 different animals, unless otherwise indicated. Data reported in the text are generally shown as mean ± standard error of the mean (s.e.m), unless otherwise indicated.

DATA AND SOFTWARE AVAILABILITY

Upon request to the Lead Contact, data are immediately available.

Supplementary Material

Refer to Web version on PubMed Central for supplementary material.

ACKNOWLEDGMENTS

We thank Steven Siegelbaum for generously providing *Amigo2-cre* mice, Katsuhiko Nishimori for the *Oxtr cDNA*^{HA}*-Ires-Cre* mice, and D. Olson and B. Lowell for the *Oxytocin-IRES-Cre* mice. We thank Scott Owen for valuable comments on the manuscript and Jayeeta Basu for expert technical advice. This work was supported by research grants from the Ford Foundation (pre-doctoral fellowship) and NINDS (1F99NS108552) (to K.W.E.); from NINDS (NS24067), NIMH (MH64070), and the Druckenmiller, Simons, Mathers, and Burnett Family Foundations (to R.W.T.); from a Sloan Fellowship (to R.C.F.), a Pew Scholarship (to R.C.F.), a McKnight Scholarship (to R.C.F.), and a Skirball Collaborative Research Award (to R.C.F. and M.V.C.); from NINDS (T32 NS086750 to N.N.T. and M.M.); from NIMH (K99/R00 MH106744 to I.C.); and from NINDS (NS21072) and NIA (AG025970) (to M.V.C.).

REFERENCES

Alexander GM, Farris S, Pirone JR, Zheng C, Colgin LL, and Dudek SM (2016). Social and novel contexts modify hippocampal CA2 representations of space. Nat. Commun 7, 10300. [PubMed: 26806606]

Bargmann CI, and Marder E (2013). From the connectome to brain function. Nat. Methods 10, 483–490. [PubMed: 23866325]

Baumgartner T, Heinrichs M, Vonlanthen A, Fischbacher U, and Fehr E (2008). Oxytocin shapes the neural circuitry of trust and trust adaptation in humans. Neuron 58, 639–650. [PubMed: 18498743]

Benes FM, Lim B, Matzilevich D, Subburaju S, and Walsh JP (2008). Circuitry-based gene expression profiles in GABA cells of the trisynaptic pathway in schizophrenics versus bipolars. Proc. Natl. Acad. Sci. USA 105, 20935–20940. [PubMed: 19104056]

Bley KR, and Tsien RW (1990). Inhibition of Ca2+ and K+ channels in sympathetic neurons by neuropeptides and other ganglionic transmitters. Neuron 4, 379–391. [PubMed: 1690565]

Botcher NA, Falck JE, Thomson AM, and Mercer A (2014). Distribution of interneurons in the CA2 region of the rat hippocampus. Front. Neuroanat 8, 104. [PubMed: 25309345]

Brown DA, and Adams PR (1980). Muscarinic suppression of a novel voltage-sensitive K+ current in a vertebrate neurone. Nature 283, 673–676. [PubMed: 6965523]

Brown BS, and Yu SP (2000). Modulation and genetic identification of the M channel. Prog. Biophys. Mol. Biol 73, 135–166. [PubMed: 10958929]

Cantrell AR, and Catterall WA (2001). Neuromodulation of Na+ channels: an unexpected form of cellular plasticity. Nat. Rev. Neurosci 2, 397–407. [PubMed: 11389473]

Cantrell AR, Ma JY, Scheuer T, and Catterall WA (1996). Muscarinic modulation of sodium current by activation of protein kinase C in rat hippocampal neurons. Neuron 16, 1019–1026. [PubMed: 8630240]

Cardin JA, Carlén M, Meletis K, Knoblich U, Zhang F, Deisseroth K, Tsai LH, and Moore CI (2009). Driving fast-spiking cells induces gamma rhythm and controls sensory responses. Nature 459, 663–667. [PubMed: 19396156]

Carr DB, Day M, Cantrell AR, Held J, Scheuer T, Catterall WA, and Surmeier DJ (2003). Transmitter modulation of slow, activity-dependent alterations in sodium channel availability endows neurons with a novel form of cellular plasticity. Neuron 39, 793–806. [PubMed: 12948446]

Chen Y, Yu FH, Surmeier DJ, Scheuer T, and Catterall WA (2006). Neuromodulation of Na+ channel slow inactivation via cAMP-dependent protein kinase and protein kinase C. Neuron 49, 409–420. [PubMed: 16446144]

Chevaleyre V, and Piskorowski RA (2016). Hippocampal Area CA2: An Overlooked but Promising Therapeutic Target. Trends Mol. Med 22, 645–655. [PubMed: 27372610]

Chevaleyre V, and Siegelbaum SA (2010). Strong CA2 pyramidal neuron synapses define a powerful disynaptic cortico-hippocampal loop. Neuron 66, 560–572. [PubMed: 20510860]

Choe HK, Reed MD, Benavidez N, Montgomery D, Soares N, Yim YS, and Choi GB (2015). Oxytocin Mediates Entrainment of Sensory Stimuli to Social Cues of Opposing Valence. Neuron 87, 152–163. [PubMed: 26139372]

Cui Z, Gerfen CR, and Young WS 3rd (2013). Hypothalamic and other connections with dorsal CA2 area of the mouse hippocampus. J. Comp. Neurol 521, 1844–1866. [PubMed: 23172108]

Dudek SM, Alexander GM, and Farris S (2016). Rediscovering area CA2: unique properties and functions. Nat. Rev. Neurosci 17, 89–102. [PubMed: 26806628]

Evans PR, Lee SE, Smith Y, and Hepler JR (2014). Postnatal developmental expression of regulator of G protein signaling 14 (RGS14) in the mouse brain. J. Comp. Neurol 522, 186–203. [PubMed: 23817783]

Ferguson JN, Aldag JM, Insel TR, and Young LJ (2001). Oxytocin in the medial amygdala is essential for social recognition in the mouse. J. Neurosci 21, 8278–8285. [PubMed: 11588199]

Gimpl G, and Fahrenholz F (2001). The oxytocin receptor system: structure, function, and regulation. Physiol. Rev 81, 629–683. [PubMed: 11274341]

Golomb D, Yue C, and Yaari Y (2006). Contribution of persistent Na+ current and M-type K+ current to somatic bursting in CA1 pyramidal cells: combined experimental and modeling study. J. Neurophysiol 96, 1912–1926. [PubMed: 16807352]

Heiss JE, Katz Y, Ganmor E, and Lampl I (2008). Shift in the balance between excitation and inhibition during sensory adaptation of S1 neurons. J. Neurosci 28, 13320–13330. [PubMed: 19052224]

Hernandez CC, Zaika O, Tolstykh GP, and Shapiro MS (2008). Regulation of neural KCNQ channels: signalling pathways, structural motifs and functional implications. J. Physiol 586, 1811–1821. [PubMed: 18238808]

Hidema S, Fukuda T, Hiraoka Y, Mizukami H, Hayashi R, Otsuka A, Suzuki S, Miyazaki S, and Nishimori K (2016). Generation of Oxtr cDNA(HA)-Ires-Cre Mice for Gene Expression in an Oxytocin Receptor Specific Manner. J. Cell. Biochem 117, 1099–1111. [PubMed: 26442453]

Hitti FL, and Siegelbaum SA (2014). The hippocampal CA2 region is essential for social memory. Nature 508, 88–92. [PubMed: 24572357]

Insel TR (2010). The challenge of translation in social neuroscience: a review of oxytocin, vasopressin, and affiliative behavior. Neuron 65, 768–779. [PubMed: 20346754]

Irani BG, Donato J Jr., Olson DP, Lowell BB, Sacktor TC, Reyland ME, Tolson KP, Zinn AR, Ueta Y, Sakata I, et al. (2010). Distribution and neurochemical characterization of protein kinase C-theta and -delta in the rodent hypothalamus. Neuroscience 170, 1065–1079. [PubMed: 20691763]

Jacob S, Brune CW, Carter CS, Leventhal BL, Lord C, and Cook EH Jr. (2007). Association of the oxytocin receptor gene (OXTR) in Caucasian children and adolescents with autism. Neurosci. Lett 417, 6–9. [PubMed: 17383819]

Jones MW, and McHugh TJ (2011). Updating hippocampal representations: CA2 joins the circuit. Trends Neurosci. 34, 526–535. [PubMed: 21880379]

Kaczmarek LK, and Levitan IB (1987). Neuromodulation: the biochemical control of neuronal excitability (New York: Oxford University Press).

Kay K, Sosa M, Chung JE, Karlsson MP, Larkin MC, and Frank LM (2016). A hippocampal network for spatial coding during immobility and sleep. Nature 531, 185–190. [PubMed: 26934224]

Klyachko VA, and Stevens CF (2006). Excitatory and feed-forward inhibitory hippocampal synapses work synergistically as an adaptive filter of natural spike trains. PLoS Biol. 4, e207. [PubMed: 16774451]

Kohara K, Pignatelli M, Rivest AJ, Jung HY, Kitamura T, Suh J, Frank D, Kajikawa K, Mise N, Obata Y, et al. (2014). Cell type-specific genetic and optogenetic tools reveal hippocampal CA2 circuits. Nat. Neurosci 17, 269–279. [PubMed: 24336151]

Lee SE, Simons SB, Heldt SA, Zhao M, Schroeder JP, Vellano CP, Cowan DP, Ramineni S, Yates CK, Feng Y, et al. (2010). RGS14 is a natural suppressor of both synaptic plasticity in CA2 neurons and hippocampal-based learning and memory. Proc. Natl. Acad. Sci. USA 107, 16994–16998. [PubMed: 20837545]

Lin L, Chen G, Kuang H, Wang D, and Tsien JZ (2007). Neural encoding of the concept of nest in the mouse brain. Proc. Natl. Acad. Sci. USA 104, 6066–6071. [PubMed: 17389405]

Lin YT, Hsieh TY, Tsai TC, Chen CC, Huang CC, and Hsu KS (2018). Conditional Deletion of Hippocampal CA2/CA3a Oxytocin Receptors Impairs the Persistence of Long-Term Social Recognition Memory in Mice. J. Neurosci 38, 1218–1231. [PubMed: 29279308]

Lisman JE (1997). Bursts as a unit of neural information: making unreliable synapses reliable. Trends Neurosci 20, 38–43. [PubMed: 9004418]

Liu W, Pappas GD, and Carter CS (2005). Oxytocin receptors in brain cortical regions are reduced in haploinsufficient (+/−) reeler mice. Neurol. Res 27, 339–345. [PubMed: 15949229]

Lorente De Nó R (1934). Studies on the structure of the cerebral cortex. II, Continuation of the study of the ammonic system. J. Psychol. Neurol 46, 113–177.

Lu L, Igarashi KM, Witter MP, Moser EI, and Moser MB (2015). Topography of Place Maps along the CA3-to-CA2 Axis of the Hippocampus. Neuron 87, 1078–1092. [PubMed: 26298277]

Madisen L, Zwingman TA, Sunkin SM, Oh SW, Zariwala HA, Gu H, Ng LL, Palmiter RD, Hawrylycz MJ, Jones AR, et al. (2010). A robust and high-throughput Cre reporting and characterization system for the whole mouse brain. Nat. Neurosci 13, 133–140. [PubMed: 20023653]

Marder E (2012). Neuromodulation of neuronal circuits: back to the future. Neuron 76, 1–11. [PubMed: 23040802]

Marlin BJ, Mitre M, D'amour JA, Chao MV, and Froemke RC (2015). Oxytocin enables maternal behaviour by balancing cortical inhibition. Nature 520, 499–504. [PubMed: 25874674]

Mercer A, Eastlake K, Trigg HL, and Thomson AM (2012). Local circuitry involving parvalbumin-positive basket cells in the CA2 region of the hippocampus. Hippocampus 22, 43–56. [PubMed: 20882544]

Mitre M, Marlin BJ, Schiavo JK, Morina E, Norden SE, Hackett TA, Aoki CJ, Chao MV, and Froemke RC (2016). A Distributed Network for Social Cognition Enriched for Oxytocin Receptors. J. Neurosci 36, 2517–2535. [PubMed: 26911697]

Modahl C, Green L, Fein D, Morris M, Waterhouse L, Feinstein C, and Levin H (1998). Plasma oxytocin levels in autistic children. Biol. Psychiatry 43, 270–277. [PubMed: 9513736]

Nakajima M, Görlich A, and Heintz N (2014). Oxytocin modulates female sociosexual behavior through a specific class of prefrontal cortical interneurons. Cell 159, 295–305. [PubMed: 25303526]

Nishimori K, Takayanagi Y, Yoshida M, Kasahara Y, Young LJ, and Kawamata M (2008). New aspects of oxytocin receptor function revealed by knockout mice: sociosexual behaviour and control of energy balance. Prog. Brain Res 170, 79–90. [PubMed: 18655874]

Nullmeier S, Panther P, Dobrowolny H, Frotscher M, Zhao S, Schwegler H, and Wolf R (2011). Region-specific alteration of GABAergic markers in the brain of heterozygous reeler mice. Eur. J. Neurosci 33, 689–698. [PubMed: 21226776]

Oettl LL, Ravi N, Schneider M, Scheller MF, Schneider P, Mitre M, da Silva Gouveia M, Froemke RC, Chao MV, Young WS, et al. (2016). Oxytocin Enhances Social Recognition by Modulating Cortical Control of Early Olfactory Processing. Neuron 90, 609–621. [PubMed: 27112498]

Owen SF, Tuncdemir SN, Bader PL, Tirko NN, Fishell G, and Tsien RW (2013). Oxytocin enhances hippocampal spike transmission by modulating fast-spiking interneurons. Nature 500, 458–462. [PubMed: 23913275]

Pagani JH, Zhao M, Cui Z, Avram SK, Caruana DA, Dudek SM, and Young WS (2015). Role of the vasopressin 1b receptor in rodent aggressive behavior and synaptic plasticity in hippocampal area CA2. Mol. Psychiatry 20, 490–499. [PubMed: 24863146]

Peñagarikano O, Lazaro MT, Lu XH, Gordon A, Dong H, Lam HA, Peles E, Maidment NT, Murphy NP, Yang XW, et al. (2015). Exogenous and evoked oxytocin restores social behavior in the Cntnap2 mouse model of autism. Sci. Transl. Med 7, 271ra8.

Penn DL, Sanna LJ, and Roberts DL (2008). Social cognition in schizophrenia: an overview. Schizophr. Bull 34, 408–411. [PubMed: 18375928]

Piskorowski RA, and Chevaleyre V (2013). Delta-opioid receptors mediate unique plasticity onto parvalbumin-expressing interneurons in area CA2 of the hippocampus. J. Neurosci 33, 14567–14578. [PubMed: 24005307]

Piskorowski RA, Nasrallah K, Diamantopoulou A, Mukai J, Hassan SI, Siegelbaum SA, Gogos JA, and Chevaleyre V (2016). Age-Dependent Specific Changes in Area CA2 of the Hippocampus and Social Memory Deficit in a Mouse Model of the 22q11.2 Deletion Syndrome. Neuron 89, 163–176. [PubMed: 26748091]

Pobbe RL, Pearson BL, Defensor EB, Bolivar VJ, Young WS 3rd, Lee HJ, Blanchard DC, and Blanchard RJ (2012). Oxytocin receptor knockout mice display deficits in the expression of autism-related behaviors. Horm. Behav 61, 436–444. [PubMed: 22100185]

Raam T, McAvoy KM, Besnard A, Veenema AH, and Sahay A (2017). Hippocampal oxytocin receptors are necessary for discrimination of social stimuli. Nat. Commun 8, 2001. [PubMed: 29222469]

Raggenbass M, Alberi S, Zaninetti M, Pierson P, and Dreifuss JJ (1998). Vasopressin and oxytocin action in the brain: cellular neurophysiological studies. Prog. Brain Res 119, 263–273. [PubMed: 10074793]

Sala M, Braida D, Lentini D, Busnelli M, Bulgheroni E, Capurro V, Finardi A, Donzelli A, Pattini L, Rubino T, et al. (2011). Pharmacologic rescue of impaired cognitive flexibility, social deficits, increased aggression, and seizure susceptibility in oxytocin receptor null mice: a neurobehavioral model of autism. Biol. Psychiatry 69, 875–882. [PubMed: 21306704]

Shinohara Y, Hosoya A, Yahagi K, Ferecskó AS, Yaguchi K, Sík A, Itakura M, Takahashi M, and Hirase H (2012). Hippocampal CA3 and CA2 have distinct bilateral innervation patterns to CA1 in rodents. Eur. J. Neurosci 35, 702–710. [PubMed: 22339771]

Siegelbaum SA, and Tsien RW (1983). Modulation of gated ion channels as a mode of transmitter action. Trends Neurosci. 6, 307–313.

Striepens N, Kendrick KM, Maier W, and Hurlemann R (2011). Prosocial effects of oxytocin and clinical evidence for its therapeutic potential. Front. Neuroendocrinol 32, 426–450. [PubMed: 21802441]

Suh BC, Horowitz LF, Hirdes W, Mackie K, and Hille B (2004). Regulation of KCNQ2/KCNQ3 current by G protein cycling: the kinetics of receptor-mediated signaling by Gq. J. Gen. Physiol 123, 663–683. [PubMed: 15173220]

Takano K, Stanfield PR, Nakajima S, and Nakajima Y (1995). Protein kinase C-mediated inhibition of an inward rectifier potassium channel by substance P in nucleus basalis neurons. Neuron 14, 999–1008. [PubMed: 7538311]

Takayanagi Y, Yoshida M, Bielsky IF, Ross HE, Kawamata M, Onaka T, Yanagisawa T, Kimura T, Matzuk MM, Young LJ, and Nishimori K (2005). Pervasive social deficits, but normal parturition,

in oxytocin receptor-deficient mice. Proc. Natl. Acad. Sci. USA 102, 16096–16101. [PubMed: 16249339]

Tamamaki N, Abe K, and Nojyo Y (1988). Three-dimensional analysis of the whole axonal arbors originating from single CA2 pyramidal neurons in the rat hippocampus with the aid of a computer graphic technique. Brain Res. 452, 255–272. [PubMed: 3401733]

Telezhkin V, Reilly JM, Thomas AM, Tinker A, and Brown DA (2012). Structural requirements of membrane phospholipids for M-type potassium channel activation and binding. J. Biol. Chem 287, 10001–10012. [PubMed: 22303005]

Tomizawa K, Iga N, Lu YF, Moriwaki A, Matsushita M, Li ST, Miyamoto O, Itano T, and Matsui H (2003). Oxytocin improves long-lasting spatial memory during motherhood through MAP kinase cascade. Nat. Neurosci 6, 384–390. [PubMed: 12598900]

Uhrig S, Hirth N, Broccoli L, von Wilmsdorff M, Bauer M, Sommer C, Zink M, Steiner J, Frodl T, Malchow B, et al. (2016). Reduced oxytocin receptor gene expression and binding sites in different brain regions in schizophrenia: A post-mortem study. Schizophr. Res 177, 59–66. [PubMed: 27132494]

Wang HS, Pan Z, Shi W, Brown BS, Wymore RS, Cohen IS, Dixon JE, and McKinnon D (1998). KCNQ2 and KCNQ3 potassium channel subunits: molecular correlates of the M-channel. Science 282, 1890–1893. [PubMed: 9836639]

Wu S, Jia M, Ruan Y, Liu J, Guo Y, Shuang M, Gong X, Zhang Y, Yang X, and Zhang D (2005). Positive association of the oxytocin receptor gene (OXTR) with autism in the Chinese Han population. Biol. Psychiatry 58, 74–77. [PubMed: 15992526]

Wu Y, Lu W, Lin W, Leng G, and Feng J (2012). Bifurcations of emergent bursting in a neuronal network. PLoS ONE 7, e38402. [PubMed: 22685566]

Wuttke TV, Seebohm G, Bail S, Maljevic S, and Lerche H (2005). The new anticonvulsant retigabine favors voltage-dependent opening of the Kv7.2 (KCNQ2) channel by binding to its activation gate. Mol. Pharmacol 67, 1009–1017. [PubMed: 15662042]

Yamada-Hanff J, and Bean BP (2015). Activation of Ih and TTX-sensitive sodium current at subthreshold voltages during CA1 pyramidal neuron firing. J. Neurophysiol. 114, 2376–2389. [PubMed: 26289465]

Zaczek R, Chorvat RJ, Saye JA, Pierdomenico ME, Maciag CM, Logue AR, Fisher BN, Rominger DH, and Earl RA (1998). Two new potent neurotransmitter release enhancers, 10,10-bis(4-pyridinylmethyl)-9(10H)-anthracenone and 10,10-bis(2-fluoro-4-pyridinylmethyl)-9(10H)-anthracenone: comparison to linopirdine. J. Pharmacol. Exp. Ther 285, 724–730. [PubMed: 9580619]

Zaninetti M, and Raggenbass M (2000). Oxytocin receptor agonists enhance inhibitory synaptic transmission in the rat hippocampus by activating interneurons in stratum pyramidale. Eur. J. Neurosci 12, 3975–3984. [PubMed: 11069593]

Zhao M, Choi YS, Obrietan K, and Dudek SM (2007). Synaptic plasticity (and the lack thereof) in hippocampal CA2 neurons. J. Neurosci 27, 12025–12032. [PubMed: 17978044]

Highlights

- Oxytocin alters intrinsic properties of CA2 pyramidal cells to induce burst firing
- OXT-driven PIP_2 hydrolysis reduces M-current and spike overshoot and undershoot
- These actions and activation of fast-spiking interneurons promote CA2 bursts
- CA2 bursts shape short-term plasticity and E:I ratio of feedforward drive onto CA1

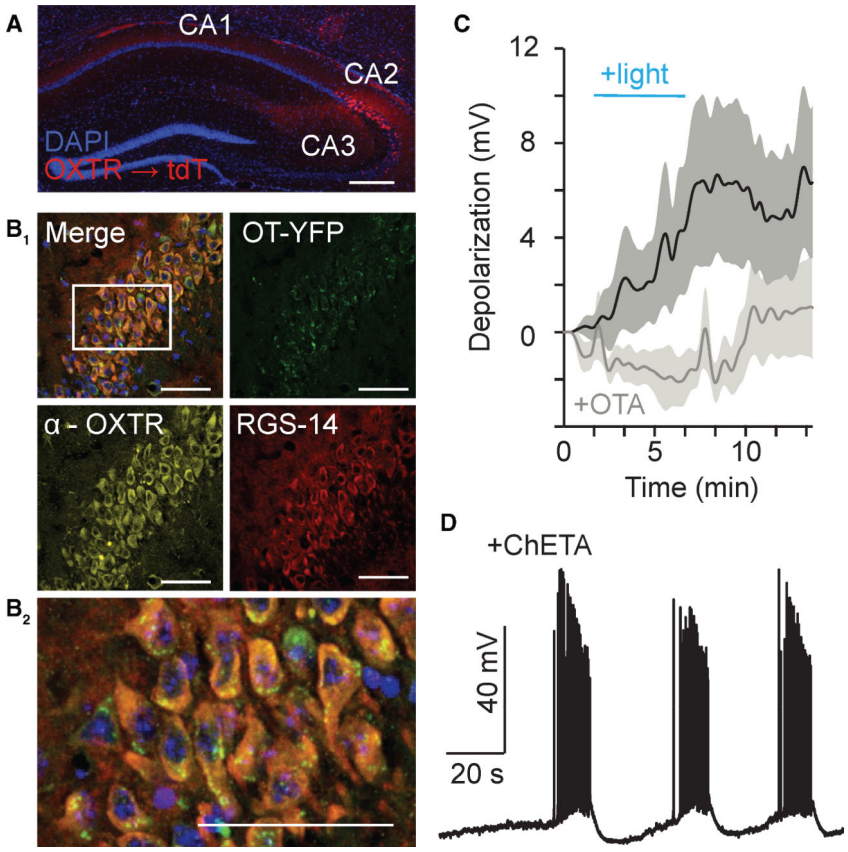

Figure 1. CA2 Pyramidal Cells Express the Oxytocin Receptor and Are Depolarized by Optogenetic Activation of Oxytocinergic Axon

(A) TdTomato expression (red) driven by the *Oxtr* promoter in hippocampal slices (DAPI-stained nuclei). Note strong labeling in the pyramidal layer of CA2 and the neighboring CA3. Scale bar, 200 μm.

(B_1) CA2 pyramidal cells, identified by RGS14 (red), co-expressed OXTR (yellow) with YFP+ oxytocinergic fibers (green) on somata. Scale bars, 50 μm.

(B_2) Magnification of the boxed section in B_1. Scale bar, 50 μm.

(C) Depolarization to blue light stimulation in CA2 pyramidal neurons of hippocampal slices expressing CheTA-YFP (black trace) was blocked by pre-incubation with 1 μM OTA (gray trace; unpaired Student's t test, $p > 0.15$). Membrane depolarization was quantified as the average change in membrane potential 6–8 min after stimulus onset (membrane potential low pass-filtered to prevent spike contamination). SEM depolarization shown in gray with the mean overlaid.

(D) Example burst firing in a CA2 pyramidal cell after 5 min of light stimulation (5 Hz) of ChETA+ oxytocinergic fibers.

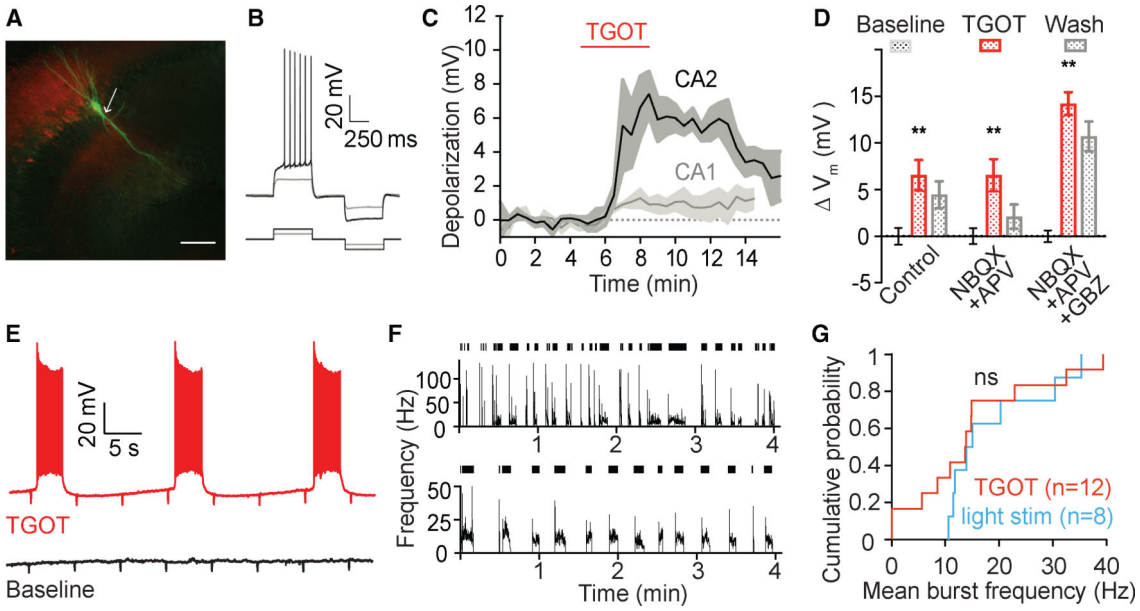

Figure 2. Responses of CA2 Pyramidal Cells to Oxytocin Receptor Stimulation by TGOT

(A) Biocytin-filled CA2 pyramidal cell with an apical dendrite bifurcation near the soma (arrow). The pyramidal neuron displayed Amigo2-Cre driven expression of AAV Cre-dependent TdTomato (red). Scale bar, 100 μm.

(B) CA2 pyramidal cells fired delayed action potentials to a depolarizing current step and showed minimal sag to a hyperpolarizing current step.

(C) Passive current clamp recordings (zero applied current) in the presence of the excitatory blockers NBQX (10 μM) and AP5 (50 μM) revealed that TGOT (400 nM) depolarized CA2 pyramidal cells; CA1 pyramidal cells showed minimal direct depolarization. SEM depolarization shown in gray with the mean overlaid.

(D) CA2 pyramidal cells depolarized to TGOT similarly without (left) or with excitatory blockers (center, NBQX and APV); depolarization was significantly greater with excitatory and inhibitory blockade (right). Data are baseline-subtracted by the pre-TGOT resting membrane potential. **$p < 0.01$.

(E) Exemplar current clamp recording of spike bursts induced by TGOT application.

(F) Spike rasters for two cells (vertical bars) and corresponding instantaneous frequency (black traces) during TGOT application (4 min).

(G) Cumulative frequency distributions of evoked firing in CA2 cells driven by application of TGOT (red) or within 30 min of optogenetically driven release of endogenous oxytocin (black); the median frequencies are similar (~15 Hz).

All error bars reflect the SEM.

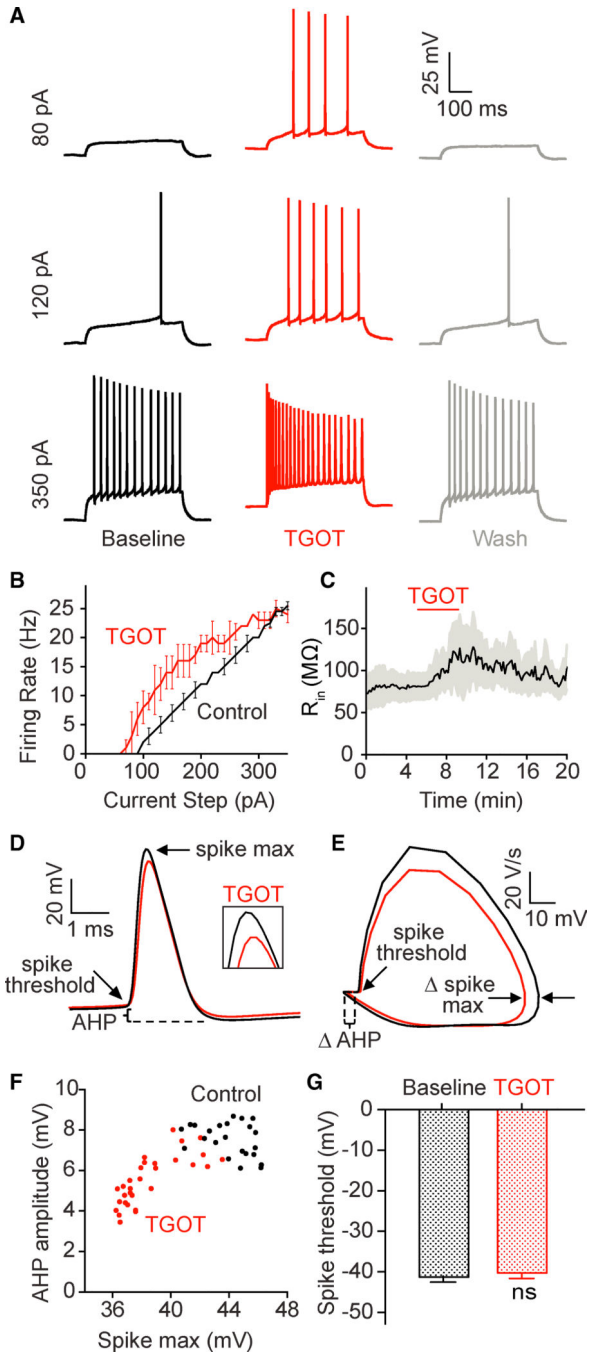

Figure 3. TGOT Increases CA2 Pyramidal Cell Excitability and Alters Spike Shape

(A) Current steps of increasing amplitude applied during whole-cell recordings from CA2 pyramidal cells in the presence of TGOT (red).

(B) Exemplar frequency-current (F-I) curve from a CA2 pyramidal cell showing a leftward shift in response to TGOT application. The neuron was initially current-clamped to −70 mV to prevent spontaneous spikes; the holding current held steady throughout the recording. Group data are shown in Figure 4B.

(C) CA2 input resistance increase following TGOT application. SEM depolarization shown in gray with the mean overlaid.
(D) Average spike waveform generated by a current injection in an exemplar cell during control (black) and TGOT application (red). TGOT decreases spike amplitude and after-hyperpolarization. The spike peak is highlighted in the inset (box size, 0.5 ms wide and 10 mV tall).
(E) Phase plane plot of the average action potential waveform shown in (D).
(F) Spike amplitude and after-hyperpolarization both decrease during TGOT application and are correlated.
(G) Spike threshold is unchanged with TGOT.
All error bars are the SEM.

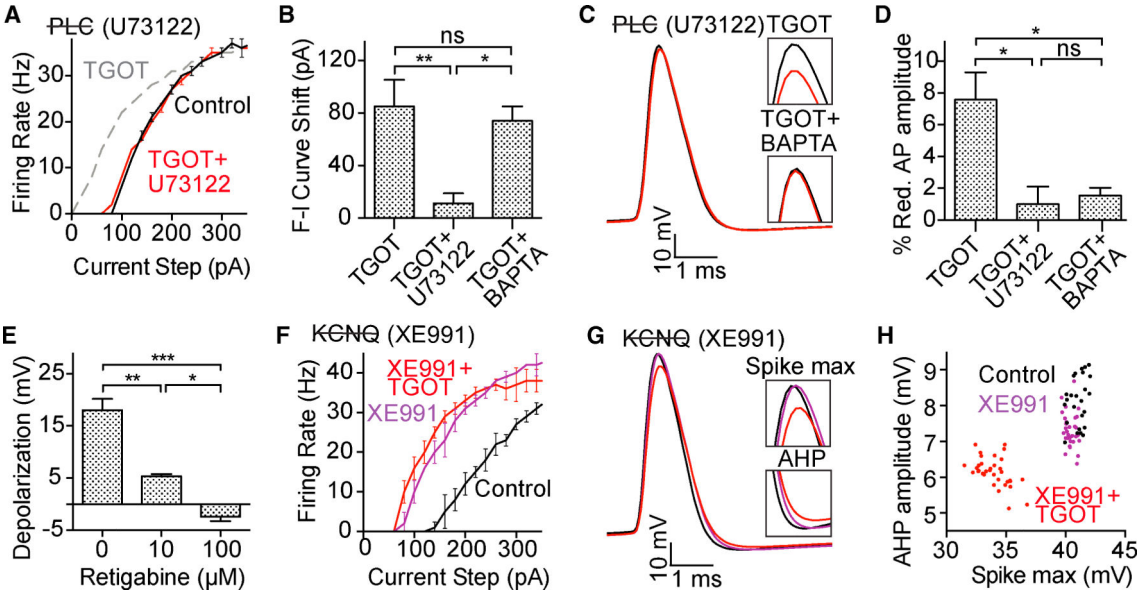

Figure 4. OXTR Signaling via PLC and KCNQ Channel Function Are Necessary for Changes in CA2 Pyramidal Cell-Intrinsic Properties

(A) The presence of the PLC blocker U73122 prevented the TGOT-induced leftward shift in the F-I curve. Baseline (black), TGOT+U73122 (red), and TGOT alone (gray dashed) curves are compared.

(B) The F-I curve shift was quantified by fitting second-order polynomial curves to interpolate the current inputs required to generate 10-Hz firing at baseline and in the presence of drug. The F-I curve shift was blocked by U73122 but not by BAPTA (20 mM) in the recording pipette.

(C) Average spike waveform generated by current injection during control (black) and TGOT plus U73122 (red) conditions. U73122 blocked the reduction in spike amplitude caused by TGOT, as did BAPTA in the recording pipette. Spike peaks are highlighted in the inset (box size, 0.5 ms wide and 10 mV tall).

(D) Summary of the percent reduction in action potential amplitude between baseline and drug conditions.

(E) Retigabine prevented TGOT-induced depolarization in a dose-dependent manner; 100 μM Retigabine prevented CA2 pyramidal cell depolarization during TGOT application.

(F) XE991 caused a leftward shift of the F-I curve that occluded TGOT's effect on excitability.

(G) Average spike waveform generated by current injection during control (black), XE991 alone (blue), and XE991 with TGOT (red) conditions in an example cell. Spike peak and after-hyperpolarization (AHP) are highlighted in the insets (0.5 ms wide, 10 mV tall).

(H) XE991 was not sufficient to alter spike shape; XE991 alone (violet) did not decrease spike amplitude or after-hyperpolarization although subsequent application of TGOT (red) did.

All error bars reflect the SEM. *$p < 0.05$, **$p < 0.01$, ***$p < 0.001$. See also Figure S3.

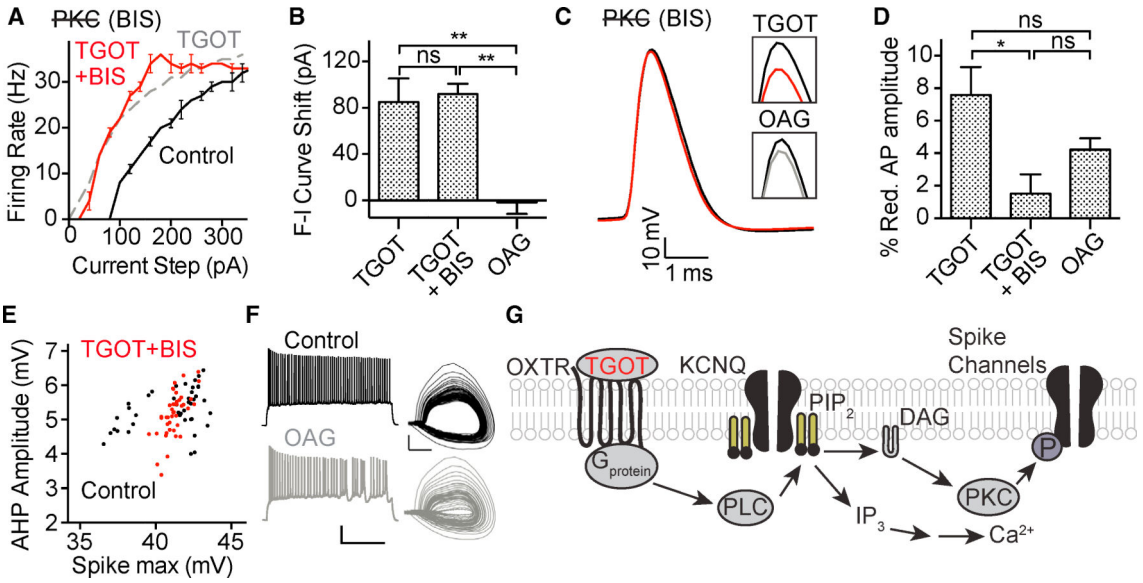

Figure 5. OTR Signaling via PKC Is Not Required for TGOT-Induced Changes in Excitability but Is Required for Changes in Spike Shape

(A) Application of TGOT in the presence of the PKC blocker BIS did not affect the shift in the F-I curve. Baseline (black), TGOT plus BIS (red), and TGOT alone (gray dashed) curves are shown for comparison in this example cell.

(B) Quantification of the shift in the F-I curve; BIS application did not prohibit the TGOT-induced increase in excitability, and PKC activation alone (via OAG) failed to increase cell excitability.

(C) Average spike waveforms show that blocking PKC activation with BIS prohibited changes in spike configuration. The insets highlight spike amplitude changes because TGOT alone (red) and OAG alone (gray).

(D) Summary of percent reduction in spike amplitude between baseline and drug conditions.

(E) Spike amplitude and after-hyperpolarization were not reduced by TGOT when PKC activity was blocked.

(F) Responses to the 12th in a series of current injections (left) and corresponding phase plane plots (right) point to enhanced slow inactivation of spike channels during OAG application in the CA2 pyramidal cell. Scale bars, 20 mV (horizontal), 40 V/s (vertical).

(G) Proposed mechanism underlying TGOT action on CA2 pyramidal cells. TGOT activates OXTRs; an intermediary G-protein activates PLC, which degrades PIP_2 into inositol triphosphate (IP_3) and DAG; depletion of PIP_2 from the cell membrane results in closing of KCNQ channels, increasing the membrane resistance and allowing depolarization; DAG activates PKC; and PKC may phosphorylate spike channels (likely Na^+ channels), reducing peak conductance and increased slow inactivation.

All error bars reflect the SEM. *$p < 0.05$, **$p < 0.01$. See also Figure S4.

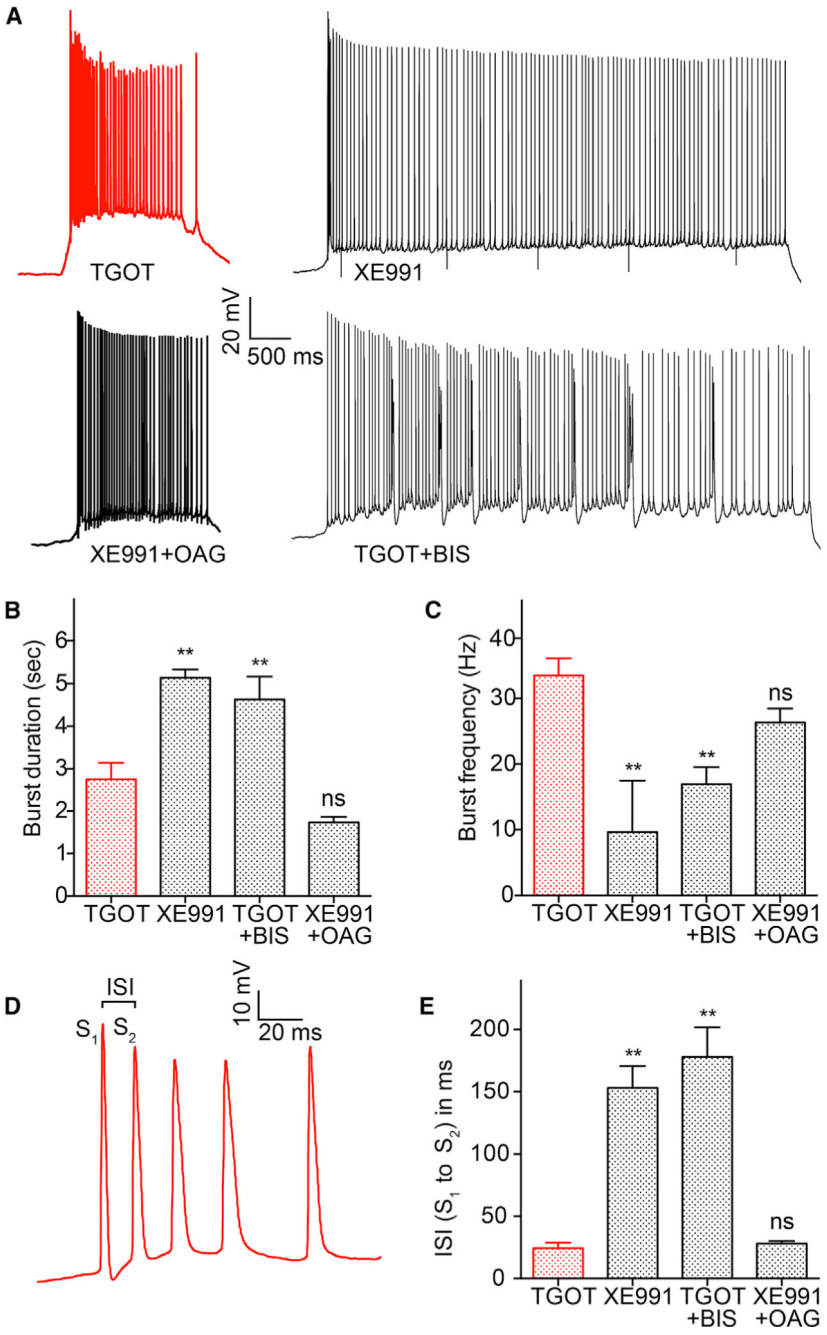

Figure 6. TGOT-Induced Bursting Is Shaped by Both KCNQ Conductance and PKC Action on Excitatory Current

(A) Exemplar bursts recorded from CA2 pyramidal cells In the presence of TGOT, the KCNQ channel blocker XE991, TGOT plus the PKC blocker BIS, and the KCNQ blocker plus the PKC activator OAG.

(B) Average burst duration.

(C) Average burst frequency.

(D) Magnification of spikes early in a burst during TGOT application, indicating the initial interspike interval between the first (S_1) and second (S_2) spikes.

(E) Mimicry of the brief ISI in TGOT was not obtained with XE991 or TGOT plus BIS but was achieved upon PKC activation with OAG.
All error bars reflect the SEM. **p < 0.01.

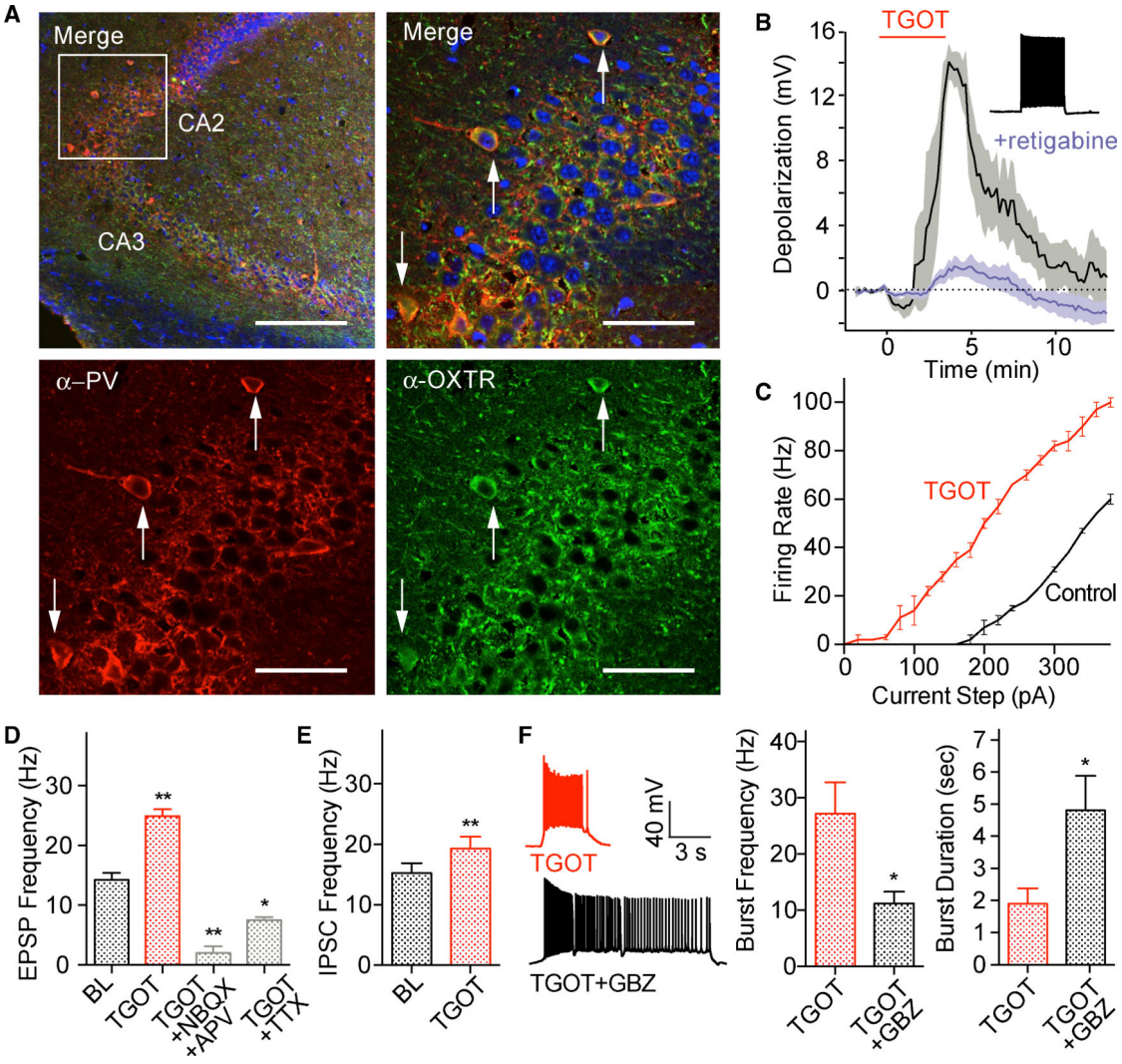

Figure 7. CA2 Fast-Spiking Cells Are Also Activated by TGOT and Help Sculpt Pyramidal Cell Activity

(A) Parvalbumin-positive interneurons (red) were expressed at a high density in CA2 and generally expressed OXTR. Box, top left, the magnified area at the right and bottom. Scale bars, 250 μm (top left), 50 μm elsewhere. Analysis of OXTR immunoreactivity was performed when the cell body could clearly be distinguished (arrows). The proportion of PV + neurons that were also OXTR+ was 55% for CA2 (n = 20), 85.7% for CA1 (n = 21), and, thus, 70.5% for both regions together (n = 44).

(B) Whole-cell recordings from PV+ fast-spiking interneurons in the CA2 region, identified using a transgenic PV-Cre reporter line and by their response to a current injection (inset), depolarized in response to TGOT application (400 nM). Data were acquired without excitatory blockers. Depolarization was largely prevented by pre-incubation with 100 μM retigabine (blue).

(C) TGOT increased excitability in fast-spiking interneurons, as shown by a leftward shift in the F-I curve of this exemplar cell.

(D) TGOT application increased EPSP frequency in fast-spiking CA2 interneurons; this increase was blocked by NBQX and APV and reduced by TTX.
(E) TGOT application increased IPSC frequency onto CA2 pyramidal cells.
(F) Example of TGOT-driven bursts in CA2 pyramidal cells during control (red) and gabazine (black) conditions. Blocking inhibition with gabazine decreased the burst frequency (center) and increased TGOT-driven burst duration (right).
All error bars reflect the SEM. *$p < 0.05$, **$p < 0.01$. See also Figure S6.

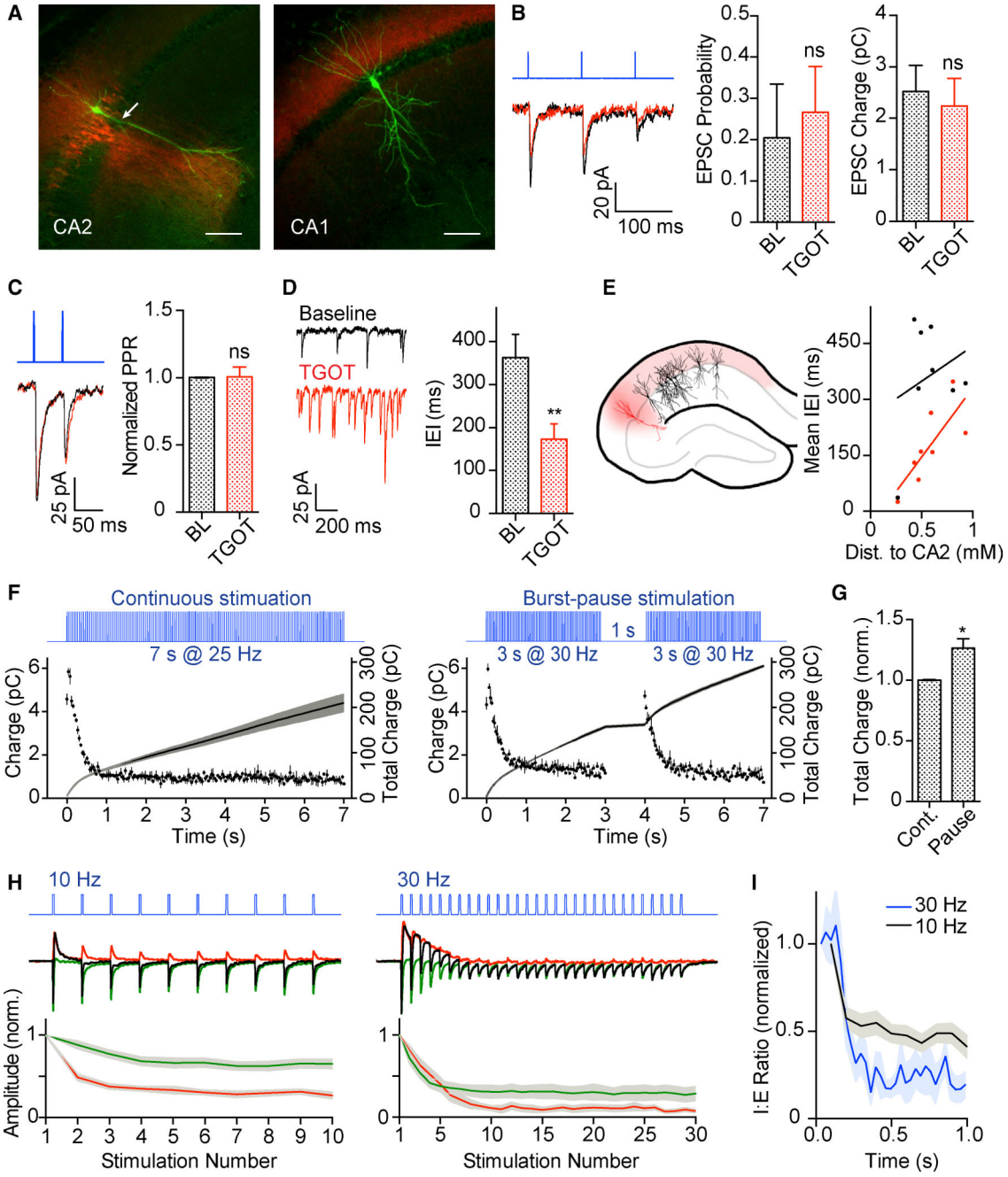

Figure 8. Properties of CA2 Output onto CA1 Pyramidal Cells and the Effects of TGOT

(A) *Amigo2-cre* mice expressed virally delivered mCherry-ChR2 in CA2 pyramidal cells (red). Shown are a ChR2-positive CA2 pyramidal cell (left) and a ChR2-negative CA1 pyramidal cell (right), each labeled with biocytin. Scale bars, 100 μm.

(B) Voltage-clamp recordings from CA1 pyramidal cells reveal excitatory inputs. Shown are 10-Hz stimulation trains under control (black) and TGOT (red) conditions; OXTR activation did not increase the release probability or EPSC charge.

(C) Blue light stimulation pulses spaced by a 50-ms interval revealed no change in paired-pulse ratio with TGOT.

(D) TGOT application increased spontaneous EPSCs onto CA1 pyramidal cells, as shown in a sample trace (left) and as a decrease in inter-event interval.
(E) Schematic indicating the location of biocytin-filled CA1 pyramidal cells (black) with respect to CA2 (red). The spontaneous EPSC frequency was correlated with the CA1 pyramidal cell's distance from CA2 during TGOT application (but not under control conditions).
(F) Recording from CA1 pyramidal cells under voltage clamp. CA2 axons were stimulated with blue light either continuously (25.7 Hz) or in a burst-pause pattern (3 s at 30 Hz) to deliver 180 stimulations over 7 s. The charge per stimulation (dots, left vertical axis) and cumulative charge (lines, right vertical axis) are shown (average ± SEM of 3 stimulations).
(G) The average cumulative excitatory charge transferred during burst-pause stimulation was 125% of that during continuous stimulation.
(H) Top: 1-s trains of 10- or 30-Hz blue light stimulation were delivered to CA2 axons during voltage-clamp recordings. Center: excitatory (green) and inhibitory (red) currents were derived from recorded current traces (black). Bottom: during stimulation trains at either frequency, inhibitory current amplitudes (red) showed greater depression than excitatory current amplitudes (data were normalized to the first stimulation amplitude).
(I) 30-Hz stimulation resulted in a larger decrease in the I:E ratio than 10-Hz stimulation.
All error bars reflect the SEM. *$p < 0.05$, **$p < 0.01$. See also Figure S7.

Table 1.

Distinguishing Features of CA2 and CA1 Pyramidal Neurons in This Study

Mean ± SEM	Resting Membrane Potential (mV)	Capacitance (pF)	Input Resistance (MΩ)	AP Amplitude (mV)	AP Half-Width (ms)	SAG (% of Steady State)	Bifurcation Soma (μm)
CA1 PYR	−62 ± 0.82 (19)	161 ± 6.60 (19)	147.42 ± 8.94 (19)	97.37 ± 3.93 (8)	1.02 ± 0.03 (8)	21 ± 3 (8)	193.1 ± 64.2 (6)
CA2 PYR	−65.85 ± 0.51 (45)	262.69 ± 9.12 (26)	81.42 ± 3.53 (28)	86.77 ± 1.82 (16)	1.00 ± 0.08 (16)	16 ± 1 (16)	84.3 ± 26.3 (6)
p Value	0.00065	4.907E–11	7.5172E-10	P < 0.01	n.s.	P < 0.10	p < 0.0033

*Reported values are not corrected for the ~12-mV junction potential. The number of cells in each group is indicated next to the measurement value in parentheses. Reported p values are the results of an unpaired Student's t test. n.s., not significant.

KEY RESOURCES TABLE

REAGENT or RESOURCE	SOURCE	IDENTIFIER
Antibodies		
α - PV (mouse; 1:500)	Swant	Cat# PV 25; RRID: AB_10000344
α - KCNQ3 (rabbit; 1:200)	Alomone	Cat# APC-051; RRID: AB_2040103
α - RGS14 (mouse; 1:100)	NeuroMab	Cat# 75–372; RRID: AB_2179931
α - OXTR (rabbit; 1:30, unpurified)	Froemke and Chao labs (NYU School of Medicine) Mitre et al., 2016	OXTR-2; RRID:AB_2571555
OAG (1-Oleoyl-2-acetyl-sn-glycerol; 20 μM)	Sigma Aldrich	Cat# O6754
XE-991 (10 μM)	Sigma Aldrich	Cat# X2254
TGOT ((Thr^{4},Gly^{7})-Oxytocin; 400 nM)	Bachem	Cat# 4013837
AVP ((Arg^{8})-Vasopressin trifluoroacetate salt; 1 μM)	Bachem	Cat# 4012215
Bis (Bisindolylmaleimide I; 10 μM)	Cayman Chemical	Cat# 13298
U 73122 (5 μM)	Tocris	Cat# 1268
Retigabine (10, 100 μM)	Alomone	Cat# R-100
Bacterial and Virus Strains		
pAAV5-EF1α-DIO-ChETA-eYFP	Penn Vector Core	N/A
pAAV-EF1α-dflox.hChR2(H134R)-mCherry-WPRE-hGH	Penn Vector Core	N/A
Experimental Models: Organisms/Strains		
Mouse: C57B/6J	Jackson Labs	Cat# 000664
Mouse: B6;129S-Oxttm1.1(cre)Dolsn/J (Oxt-ires-cre)	Jackson Labs	Cat# 024234
Mouse: B6.Cg-Tg(Amigo2-cre)1Sieg/J(*Amigo2-Cre*)	Jackson Labs	Cat# 030215
Mouse: Oxtr cDNA^{HA}-Ires-Cre (OXTR-Cre)	Dr. Katsuhiko Nishimori (Tohoku University)	N/A
Mouse: B6;129S6-*Gt(ROSA)26Sor$^{tm14(CAG-tdTomato)Hze}$*/J (*Ai14*)	Jackson Labs	Cat# 007908
Mouse: B6;129P2-*Pvalb$^{tm1(cre)Arbr}$*/J (*PV-Cre*)	Jackson Labs	Cat# 008069
Mouse: B6.Cg-*Gt(ROSA)26Sor$^{tm9(CAG-tdTomato)Hze}$*/J (*Ai9*)	Jackson Labs	Cat# 007909